

**UNIVERSIDADE FEDERAL DE SÃO CARLOS**  
**CENTRO DE CIÊNCIAS EXATAS E DE TECNOLOGIA**  
**DEPARTAMENTO DE ENGENHARIA DE MATERIAIS**

**CO-STUFFED QUARTZ SOLID SOLUTIONS WITH ZERO  
THERMAL EXPANSION BY SOL-GEL SYNTHESIS**

**BEATRIZ PAIVA DA FONSECA**

**SÃO CARLOS – SP**  
**2023**

# **CO-STUFFED QUARTZ SOLID SOLUTIONS WITH ZERO THERMAL EXPANSION BY SOL-GEL SYNTHESIS**

Final report presented to the Materials Engineering Department of the Federal University of São Carlos as a requirement for the degree of Bachelor in Materials Engineering.

Advisor: Prof. Dr. Edgar Dutra Zanotto

São Carlos – SP  
2023



## ATA DE DEFESA DE TRABALHO DE CONCLUSÃO DE CURSO (TCC)

**NOME:** Beatriz Paiva da Fonseca

**RA:** 769181

**TÍTULO:** Co-stuffed quartz solid solutions with zero thermal expansion by sol-gel synthesis

**ORIENTADOR(A):** Prof. Dr. Edgar Dutra Zanotto

**CO-ORIENTADOR(A):** Prof. Dr.-Ing. habil. Joachim Deubener

**DATA/HORÁRIO:** 26/06/2023, 11h

### BANCA – NOTAS:

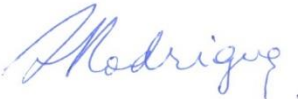
	Monografia	Defesa
Prof. Dr. Edgar Dutra Zanotto	10,0	10,0
Profa. Dra. Ana Candida Martins Rodrigues	9,5	9,5
<b>Média</b>	9,75	9,75

### BANCA – ASSINATURAS:

Prof. Dr. Edgar Dutra Zanotto

---

Profa. Dra. Ana Candida Martins



Rodrigues

---

## **ACKNOWLEDGEMENT**

First of all, I would like to thank my family for all the love: my mother Conceição, who always invested in my education, my father Walter, who always gave me courage, my sister Amanda, who is my partner and my balance, and my boyfriend Enzo, who is my supporter and role model.

I have also always been graced with good friends. Many thanks to my great friends from the beginning of my degree in Belo Horizonte Luis and Juliana (and also Arthur), whose friendship always went far beyond studies and overcame distance for years, my friends at UFSCar Carol, Franzin, Kaue, Paloma, Martinez and Pedro and all the others from the group "Primas Mancilha", and in São Carlos, Senise e Gagui, and my dear ex-roommate and professional advisor Barbara.

During my graduation I had the privilege of taking classes and being guided by great educators and professionals, whom I admire so much. I gratefully acknowledge Rosario Suman Bretas, my first advisor, and Edgar Dutra Zanotto, my advisor for this work and who made it possible for me to realize one of my greatest dreams. I would like to thank my advisors in Germany Joachim Deubener and Gundula Hensch for all the attention and knowledge taught to me, and also all my work colleagues at INW and at LaMaV, for their support.

Finally, I would like to thank all the people who have in some way cheered my success or contributed to my education.

## RESUMO

A produção de vitrocerâmicas de expansão térmica zero para além do sistema  $\text{Li}_2\text{O}\cdot\text{Al}_2\text{O}_3\cdot\text{SiO}_2$  vem despertando enorme interesse, para poupar recursos de lítio, tendo em conta as baterias emergentes à base de lítio. Os métodos de síntese de sol-gel, ou seja, *spray drying* e *dip coating*, foram usados principalmente devido à sua versatilidade e à possibilidade de produzir materiais em escala submicrométrica. A composição  $\text{CoO}\cdot\text{Al}_2\text{O}_3\cdot 4\text{SiO}_2$ , dopada com um pouco de  $\text{Li}_2\text{O}$ , foi determinada como ideal para a produção de uma solução sólida de quartzo co-recheado. Para o processo de secagem por pulverização, o metanol foi considerado o solvente adequado em vez de água. O tratamentos térmico em temperaturas acima de 800 °C permitiram a cristalização da solução sólida de quartzo Co-recheado e, acima de 900 °C, também se formou o espinélio. A formação dessa segunda fase induziu a destruturação (remoção) do cobalto no Qss. A mudança na cor do pó de acordo com a temperatura de tratamento foi observada devido à mudança de coordenação dos íons Co, que varia quando o cobalto está contido da estrutura Qss ou na estrutura de espinélio. A expansão térmica do revestimento e do pó, ambos recozidos a 900 °C, foi considerada muito próxima de zero entre 25 °C e 625 °C. Portanto, destacamos os métodos sol-gel como uma ferramenta poderosa para produzir uma solução sólida de quartzo (quase) livre de lítio com expansão térmica ajustável.

**Palavras-chave:** Síntese por sol-gel. Expansão térmica. Soluções sólidas de quartzo. Aluminossilicato de lítio. Cobalto.

## ABSTRACT

The production of zero thermal expansion glass ceramics beyond the  $\text{Li}_2\text{O}\cdot\text{Al}_2\text{O}_3\cdot\text{SiO}_2$  system has drawn enormous interest for saving lithium resources in light of the emerging Li-based batteries. Sol-gel synthesis methods, namely spray drying and dip coating, were used mainly due to their versatility and the possibility of producing materials on the sub-micrometer scale. The composition  $\text{CoO}\cdot\text{Al}_2\text{O}_3\cdot 4\text{SiO}_2$ , doped with some  $\text{Li}_2\text{O}$ , was determined to be optimal to produce Co-stuffed quartz solid solution. For the spray drying process, methanol was found to be the suitable solvent instead of water or ethanol. Heat treatments at temperatures above  $800\text{ }^\circ\text{C}$  enabled the crystallization of Co-stuffed quartz solid solution and above  $900\text{ }^\circ\text{C}$ , Spinel was also formed. The formation of this second phase induced the structural unstuffing of Co-stuffed Qss. The change in color of the powder according to the treatment temperature was observed due to the change of coordination of Co ions, which varies when the cobalt is within the Qss structure or in the spinel structure. The thermal expansion of the coating and the powder, both annealed at  $900\text{ }^\circ\text{C}$ , was found to be very close to zero between  $25\text{ }^\circ\text{C}$  and  $625\text{ }^\circ\text{C}$ . We therefore highlight sol-gel methods as a powerful toll to produce (nearly) lithium-free quartz solid solution with tuneable thermal expansion.

**Keywords:** Sol-gel synthesis. Thermal expansion. Quartz solid solutions; Lithium aluminosilicate. Cobalt.

## LIST OF ILLUSTRATIONS

Figure 1: Schematic diagram of volume versus temperature of glass and crystal material. ....	2
Figure 2: Representation of tetrahedral junctions in rings a) in quartz b) in silicate glasses .....	3
Figure 3: Scheme of the dip coating process steps.....	8
Figure 4: Scheme of the spray drying process steps .....	10
Figure 5: Network-forming character of $Al_2O_3$ .....	12
Figure 6: XRD patterns of the samples D0, D5, D9, D17, D20, D25, D33, D44 and D50.....	19
Figure 7: X-ray diffraction patterns of the samples D20.0, D20.25, D20.50, D20.75 and D20.100.....	20
Figure 8: X-ray diffraction patterns of the samples D33.0, D33.25, D33.33, D33.40, D33.45, D33.50, D33.67 and D33.100. ....	21
Figure 9: XRD results for the samples D33.100O and D33.100W. ....	22
Figure 10: Powders obtained by spray drying of the solutions: a) S0, b) S20, c) S33, d) S40, e) S50, f) S67, g) S80 and h) S100.....	22
Figure 11: XRD patterns of the samples S0, S20, S33, S40, S45, S50, S67, S80 and S100.....	23
Figure 12: Powders produced by spray drying of the solution S100M a) as-sprayed, b) after drying at 600 °C and after heat treatment at c) 800 °C, d) 850 °C, e) 900 °C, f) 950 °C and g) 1000 °C. ....	24
Figure 13: X-ray diffraction patterns of the as-sprayed S100M sample.....	24
Figure 14: X-ray diffraction patterns of the sample S100M a) dried at 600 °C, and heat-treated at c) 800 °C, d) 850 °C, e) 900 °C, f) 950 °C and g) 1000 °C.....	25



Figure 15: Dip-coated samples produced with the same solution as sample S100M. .....	26
Figure 16: Dip-coated sample (D100M) produced with the same solution as the sample S100M.....	26
Figure 17: Transmittance of the sample D100M. ....	27
Figure 18: SEM images from the samples S100M a) as-sprayed and heat-treated at b) 800 °C, c) 900 °C and d) 1000 °C.....	28
Figure 19: TEM image from as-sprayed S100M powder.....	29
Figure 20: Particle size distribution of the as-sprayed S100M sample. ....	29
Figure 21: Thermogravimetric signal and mass spectrometry of the as-sprayed S100M sample.....	30
Figure 22: Differential thermal analysis (DTA) performed on samples S100M as-sprayed, dried at 600 °C and heat-treated at 850 °C. ....	30
Figure 23: High-temperature X-ray diffraction measurements for samples S0.....	31
Figure 24: High-temperature X-ray diffraction measurements for samples S100M..	32
Figure 25: High-temperature X-ray diffraction measurements for samples D100M..	33
Figure 26: X-ray diffraction patterns from the samples LAS4 (heat-treated at 800 °C) and S100M (heat-treated at 900 °C and 1000 °C). ....	34

## LIST OF TABLES

Table 1: Composition of the solutions with different substitution percentages of $\text{SiO}_2$ by $\text{Al}_2\text{O}_3$ and $\text{CoO}$ . .....	13
Table 2: Composition of the solutions D20 with different substitution percentages of $\text{Li}_2\text{O}$ by $\text{CoO}$ . .....	14
Table 3: Composition of the solutions D33 with different substitution percentages of $\text{Li}_2\text{O}$ by $\text{CoO}$ . .....	15

## LIST OF ACRONYMS

Qss	Quartz solid solution
SCL	Supercooled liquids
Tg	Glass transition temperature
GC	Glass-ceramics
LAS	Lithium aluminosilicate ( $\text{Li}_2\text{O}\cdot\text{Al}_2\text{O}_3\cdot\text{SiO}_2$ )
HQss	High quartz structure solid solutions
CTE	Coefficient of thermal expansion
TEOS	Tetraethylorthosilicate
XRD	X-ray diffraction
Kss	Keatite solid solution
GIXRD	Grazing incidence X-ray diffraction
HT-XRD	High temperature X-ray diffraction
SEM	Scanning electron microscopy
TEM	Transmission electron microscopy
DTA	Differential thermal analysis
Tx	Temperatura de cristalização

## LIST OF SYMBOLS

$\eta$	Viscosity
$U_0$	Withdrawal speed
$\gamma$	Surface tension
$\rho$	Density
$g$	Gravitational constant

## SUMMARY

<b>1 INTRODUCTION</b> .....	<b>1</b>
<b>2 THEORETICAL FUNDAMENTALS</b> .....	<b>2</b>
2.1 GLASSES AND GLASS-CERAMICS.....	2
2.2 LAS SYSTEM.....	5
2.3 SOL-GEL TECHNOLOGY AND TEOS .....	6
2.4 DIP COATING .....	7
2.5 SPRAY DRYING .....	9
2.6 QUARTZ STRUCTURE AND LITHIUM EXCESS .....	11
<b>3 MATERIALS AND METHODS</b> .....	<b>13</b>
3.1 COMPOSITIONS.....	13
3.2 DIP COATING AND SPRAY DRYING .....	16
3.3 HEAT TREATMENTS.....	16
3.4 XRD AND HIGH TEMPERATURE XRD MEASUREMENTS.....	16
3.5 SCANNING ELECTRON MICROSCOPY (SEM) .....	17
3.6 TRANSMISSION ELECTRON MICROSCOPY (TEM) .....	17
3.7 SAMPLE TRANSMISSION MEASUREMENTS .....	17
3.8 THERMOGRAVIMETRIC ANALYSIS .....	17
<b>4 RESULTS</b> .....	<b>19</b>
4.1 REPLACEMENT OF SiO <sub>2</sub> BY Al <sub>2</sub> O <sub>3</sub> AND CoO .....	19
4.2 REPLACEMENT OF Li <sub>2</sub> O BY CoO IN THE COMPOSITION D20 .....	20
4.3 REPLACEMENT OF Li <sub>2</sub> O BY CoO IN THE COMPOSITION D33 .....	21
4.4 LITHIUM EXCESS EFFECT .....	21
4.5 REPLACEMENT OF Li <sub>2</sub> O BY CoO IN SPRAY-DRIED POWDER.....	22
4.6 INFLUENCE OF THE SOLVENT USED FOR SPRAY DRYING .....	24
4.7 XRD AND TRANSMISSION MEASUREMENTS OF D100M SAMPLES.....	25
4.8 SCANNING ELECTRON MICROSCOPE (SEM) AND TRANSMISSION ELECTRON MICROSCOPE (TEM) .....	27
4.9 THERMOGRAVIMETRIC ANALYSIS AND DIFFERENTIAL THERMAL ANALYSIS OF THE S100M POWDER.....	29
4.10 THERMAL EXPANSION BY HIGH-TEMPERATURE X-RAY DIFFRACTION.....	31
4.11 COMPARISON OF Li- AND Co-STUFFED QSS BY XRD .....	33
<b>5 DISCUSSION</b> .....	<b>35</b>
<b>6 CONCLUSIONS/FINAL CONSIDERATIONS</b> .....	<b>40</b>
<b>REFERENCES</b> .....	<b>42</b>

## 1 INTRODUCTION

Stuffed aluminosilicate quartz solid solutions (Qss) constitute a long-standing technological mainspring of state-of-the-art zero-thermal expansion glass-ceramics. Glass-ceramics are materials which present one or more crystalline phases and a glass phase, with tunable properties of both phases. Thermally invariant monolithic glass-ceramics are widely appreciated for applications ranging from fire-viewing windows to telescope mirrors, as they must have high thermal shock resistance.

There is, however, a growing demand for lithium, due to the development and production of lithium batteries, which has reduced the supply and increased the price of lithium ores (XU, 2020). Recent investigations have revealed that Qss can be synthesized over a much wider compositional landscape, by introducing divalent transition metal cations (BAZZAOUI, et al., 2023). These substitutions can also help understand the mechanism and structural characteristic behind the thermal expansion of aluminosilicate glasses and enable a compositional control over thermal expansion.

The industrial scale use of glass may however be hampered due to undeniable technological limitations. Sol-gel synthesis methods on the other hand can be used as an alternative route to obtain zero-thermal-expansion glass-ceramic powders based on Co-stuffed Qss. Aside from other advantages, they are a more energy-efficient route since the raw materials do not need to be heated at temperatures above 1000 °C. Previous works have also demonstrated that nano-sized glass materials with very promising properties can be produced (Zandona, 2021; JONSSON, ROOS and JONSON, 2010).

Hence, this work aims to answer the questions: via sol-gel synthesis, is there any composition within the  $\text{CoO}\cdot\text{Al}_2\text{O}_3\cdot\text{SiO}_2$  system which can crystallize a Co-stuffed Qss? If yes, does it have zero-thermal expansion?

## 2 THEORETICAL FUNDAMENTALS

### 2.1 GLASSES AND GLASS-CERAMICS

Glass is an intriguing material that can be found in nature, such as obsidian, the result of rapidly cooling volcanic lava, or produced in laboratories, such as anti-reflective glass and optical fibers. Although these materials have not been discovered recently, there is still much discussion about what they are (VARSHNEYA, 2013).

According to Zanotto and Mauro:

Glass is a nonequilibrium, non-crystalline condensed state of matter that exhibits a glass transition. The structure of glasses is similar to that of their parent supercooled liquids (SCL), and they spontaneously relax toward the SCL state. Their ultimate fate, in the limit of infinite time, is to crystallize (ZANOTTO and MAURO, JNCS 2017, p. 490).

This is the world's most recent definition of glass and demonstrates how complex glass is. The glass transition temperature ( $T_g$ ) is the temperature range in which the supercooled liquid structure freezes on the cooling path without crystallizing. In this range, the time of the experiment is about the same order as the intrinsic structural relaxation time, i.e., the time required for the structure to rearrange itself, which involves translational movements (ZANOTTO and MAURO, 2017). This temperature is not a characteristic of the material, it is a kinetic phenomenon that depends on the cooling or heating speed of the material (VARSHNEYA, 2013). Figure 1 illustrates this concept.

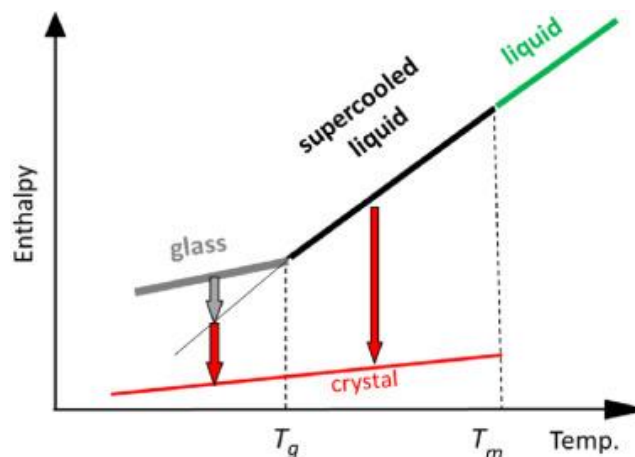


Figure 1: Schematic diagram of volume versus temperature of glass and crystal material (ZANOTTO and MAURO, 2017).

There are organic, inorganic, metallic and polymeric materials. In principle, any material can produce glass, as long as crystallization is avoided during its synthesis. However, to avoid crystallization and thus obtain a metallic glass, for example, the cooling rate required is extremely high, which hinders the production of many materials in glassy form. In this work, the focus will be primarily on inorganic oxide glasses, in particular a silicate glass.

The basic unit of silicate glasses, like the crystal of the same composition, is the tetrahedron  $\text{SiO}_4^{4-}$ , since the distance between the silicon and the oxygen and between the oxygen is the same. However, the distance between silicon changes, that is, the structure of silicate glasses differs from the of their isochemical crystal Thus, for example, in contrast to crystalline silica, which has only six-membered rings, silicate glasses have a wide distribution of ring sizes, as show in the Figure 2 (VARSHNEYA, 2013).

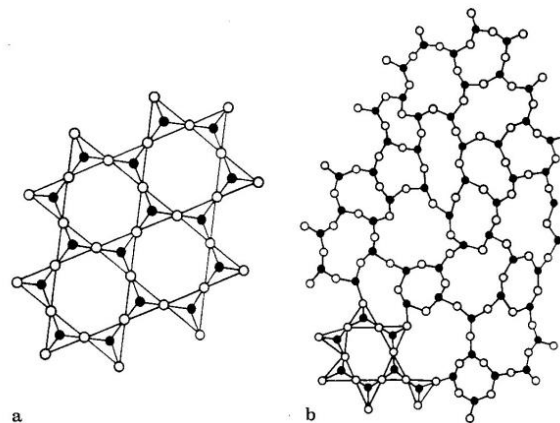


Figure 2: Representation of tetrahedral junctions in rings a) in quartz b) in silicate glasses (VOGEL, 2013).

Most applications of glasses are due to one of their several properties: *transparency*. These materials also stand out for their brightness and wide range of chemical durability, electric conductivity, thermal expansion coefficient, elastic modulus, hardness, refractive index, etc. The property that most limits the application of glass is its brittleness. Due to the enormous amount of recent research in the area, since glasses with high mechanical resistance, heat absorbing glasses, self-cleaning glasses, and electrically conductive glasses are already being manufactured (VARSHNEYA, 2013). The versatility of glass can be attributed, among other factors, to the enormous range of different compositions, since glass might be seen as



analogous to “solid” solutions (but they are not true solids). These compositional/structural characteristics allow the addition of several components to a glass formulation, for instance, in the SciGlass® database there are more than 360,000 documented glass compositions (SciGlass, 2023).

To further expand the range of applications and properties of glassy materials, glass-ceramics (GC), also known as sittals or vitroceramics, are being developed. These materials were accidentally discovered by S. Donald Stookey of Corning Glass, in 1953, after the glass he was studying was inadvertently heated in oven to 850 °C, crystallized in the volume and did not fracture after falling (HOLAND, 2019).

Vitroceramics are ceramic materials that have a residual glass phase and at least one functional crystalline phase. These materials are obtained by controlled crystallization using various methods, such as heat treatment, additive manufacturing, powder sintering and co-firing. Thus, this material class does not include spontaneously devitrified materials, whose crystallization process has not been modeled. The crystallized fraction can vary from ppm to nearly 100 % (DEUBENER, J. et al., 2018).

When it comes to glass-ceramics, crystallization can be homogeneous or heterogeneous, crystal growth can be aligned or randomly oriented, and nucleation sites can be at the surface or in the volume. All these characteristics influence the nucleation rate and the speed of crystal growth, and are therefore crucial in modeling the microstructure of these materials (DEUBENER, J. et al., 2018).

The unique properties of glass-ceramics are achieved not only by the architecture of the crystalline phase (or phases), namely the shape, distribution and composition of the crystals, but also by the characteristics of the residual glass phase, such as its composition. Besides being able to maintain transparency, glass-ceramics can have properties superior to those of the precursor glass, such as greater mechanical toughness, improved chemical durability and a higher resistance to radiation damage. In addition, due to the absence of a center of symmetry, certain properties that are not allowed in glasses and several crystals, such as piezoelectricity and the electro-optic effect, can occur in GCs (DAVIS and ZANOTTO, 2017).

Numerous commercial glass-ceramic advancements have already been introduced to the market for various domestic and high-tech applications. These include transparent and heat-resistant cookware, telescopes, artificial teeth, fire-resistant doors and windows, bioactive materials, chemically and mechanically machinable materials, as well as sealing applications and electronic and optical devices (DEUBENER, J. et al., 2018; MONTAZERIAN, SINGH and ZANOTTO, 2015).

## 2.2 LAS SYSTEM

Compositions of the ternary system  $\text{Li}_2\text{O}\cdot\text{Al}_2\text{O}_3\cdot\text{SiO}_2$  (LAS) were one of the first studied when it comes to obtaining glass-ceramics, and are still massively researched. The great interest in studying this system is due to an advantageous combination of properties that it exhibits, such as excellent chemical durability, high transparency (even after crystallization) and an excellent thermal shock resistance, due to the refractoriness up to 700 °C combined with ultra-low thermal expansion (DRESSLER, RÜDINGER and DEUBENER, 2011; REBOUÇAS, et al., 2019). The main applications of this material are for telescope mirrors, high temperature windows and cooktops plates (BUCHNER, et al, 2013).

Microstructure engineering enables the nucleation and growth of quartz solid solution (Qss) and keatite-type crystals to sizes smaller than 100 nm, which combined with the residual glass, results in a material with outstanding thermo-mechanical and optical properties (DRESSLER, RÜDINGER and DEUBENER, 2011).

In zero-expansion glass-ceramics, crystals of high quartz structure solid solutions (HQss) have negative coefficient of thermal expansion (CTE) parallel to the crystallographic c-axis. In combination with the slightly positive CTE of the residual glassy phase, the overall glass-ceramic presents zero-expansion (HELSCH, et al.; BUCHNER, et al, 2013). SCHOTT's ZERODUR®, for example, is a lithium aluminum silica glass-ceramic material, produced by controlled volume crystallization and which has a CTE equal to  $0.00 \pm 0.02 \times 10^{-6} \text{ K}^{-1}$  between 0 °C and 50 °C (ZANOTTO, 2010).

Lithium's end-use market is led by the glass and ceramic industry. Meanwhile, there has been a rise in global demand for lithium minerals with low purity in the meantime, especially for use in lithium batteries for portable electronic devices and

electric vehicles (REBOUÇAS, et al., 2019).

## 2.3 SOL-GEL TECHNOLOGY AND TEOS

Inorganic compounds and organic-inorganic hybrids can be synthesized from liquid sources using the sol-gel method. Its main advantage is that it uses low temperatures for processing, which implies no need to melt the raw materials for the production of glass (VARSHNEYA, 2013, KAJIHARA, 2013).

This synthesis route is extremely interesting for obtaining glasses that are difficult to produce by the more conventional melt-quench method, because it employs temperatures below the temperatures of maximum nucleation rate and maximum growth, and by the vapor phase method. Sol-gel synthesis enlarges the compositional range, increases the concentration of dopants, and builds tailored photo- and magnetoactive centers (VARSHNEYA, 2013, KAJIHARA, 2013).

Due to its easy application and ability to obtain crack-free thin films (up to 1  $\mu\text{m}$  thick), the sol-gel technique finds great applicability in the area of thin film deposition. Sol-gel coatings are well commercialized for several antireflective, conductive, and for corrosion, scratch, and wear protection, as well as electronic passivation (VARSHNEYA, 2013).

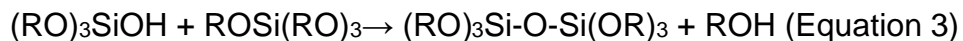
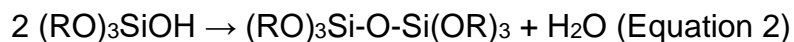
The most common reagent used in this process is a hydrolyzable silicon organometallic, namely, tetraethylorthosilicate (TEOS), tetraethoxysilane, or silicon tetraethoxide, with the formula  $\text{Si}(\text{OC}_2\text{H}_5)_4$ . To produce the colloidal suspension, the first step is to mix the appropriate quantities of reactants. Alcohol is used as a common solvent for the metalorganics and water, because they do not dissolve well together. The synthesis then starts with the hydrolysis and production of the silanol groups ( $=\text{SiOH}$ ), as shown at Equation 1 below (VARSHNEYA, 2013; KLEIN, 1985).



During this stage, the solution is stirred which, along with the high purity of the reagents, makes possible the high purity and microscale homogeneity of the final product. The reaction mechanism involved in this hydrolysis is the electrophilic substitution in the presence of an acid catalyst. When  $\text{HNO}_3$  is used as a catalyst, the excess  $\text{H}^+$  ions in the solution quickly protonate the alkoxide groups present in the

TEOS. Furthermore, water can attack the protonated group, since the electron density has been removed from the silicon atom, and thus the hydrolysis reaction is accelerated (VARSHNEYA, 2013; KLEIN, 1985).

Subsequently, right after the formation of the silanol group by hydrolysis, polymerization (or condensation) reactions are already observed. Two types of reactions are observed: water condensation, by reaction between two silane groups (Equation 2), and alcohol condensation reaction, by reaction between a silanol group and an alkyl group (Equation 3) (VARSHNEYA, 2013).



The next step is drying, to exchange the pore fluid of the gel for air. This process must be carried out carefully, because the aerogel typically has pore and network structure and this heterogeneous structure of the gels causes capillary forces of varying strength. Without control, this process can lead to cracking and collapse of the pore structure when the gel shrinks (VARSHNEYA, 2013; KLEIN, 1985).

A final optional step is to heat the material slightly above the T<sub>g</sub> of the glass, if a higher-density structure is desired. During the heating, viscous flow-assisted sintering gives rise to the gradual elimination of the porosity. Unreacted hydroxyls can also condensate during the sintering process, forming Si-O-Si bonds (VARSHNEYA, 2013; KLEIN, 1985).

## 2.4 DIP COATING

The preparation of a colloidal dispersion, or sol, is the base for sol-gel processing. Basically, the process starts with the immersion of a substrate in the solution and, after some time, proper withdrawal of it to obtain a thin solid coherent film (BRINKER, et al., 1996). The Figure 3 below illustrates the process.

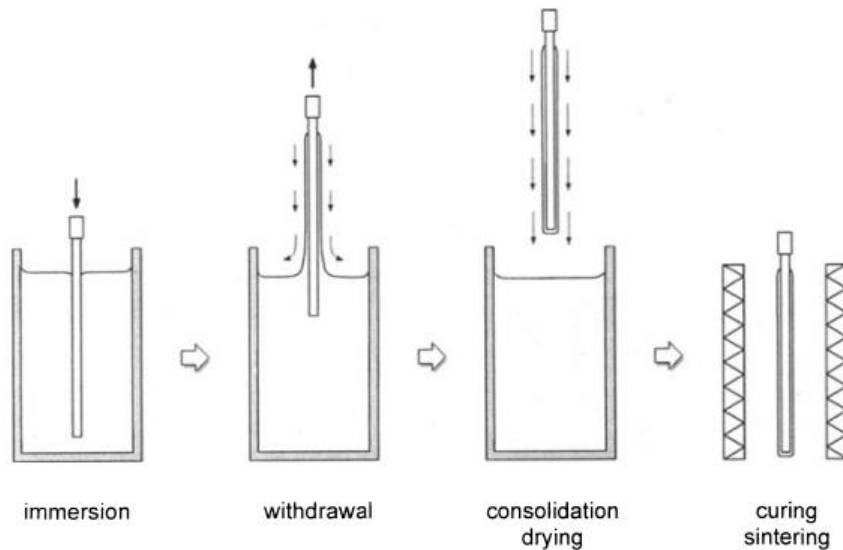


Figure 3: Scheme of the dip coating process steps (AEGERTER and MENNIG, 2013).

Obtaining coatings through dip coating is very advantageous due to the high homogeneity of the layers and the flexibility of the process, since the coated substrate can have various geometries and it is possible to produce layers of nearly any thickness. Furthermore, this process stands out because it is quick and affordable, due to the ability to form coatings of different metal oxides and to coat large substrates, making it suitable for industrial and lab applications (DISLICH and HUSSMANN, 1981).

The most common application for the dip coating method is for optical coatings, such as antireflective coatings glasses, protective layers on sensitive surfaces, and manufacture of vehicle rear mirrors. Further uses of coatings produced via dip coating process are in the field of electronic, membrane and sensor applications (DISLICH and HUSSMANN, 1981; BUTT, 2022).

In the dip coating process, the most determining events in the quality and characteristics of the deposited film occur during and after the withdrawal of the substrate. In this aspect, it is crucial to control the pulling speed and the solvent evaporation conditions, in order to obtain the desired properties (optical, geometrical, among others) and material structure. Other parameters that directly influence are density and viscosity of the solution, surface tension, substrate surface and dip-coating cycles (BUTT, 2022).

During the withdrawal stage, different forces combined results in uniformly spreading out of the solution along the surface of the substrate, namely viscous flow, draining, and capillary forces. Subsequently, the gelation of the film occurs as a result of the evaporation of the solvents used to produce the solution. In order to densify the film and also to achieve the desired properties, the film can be heat treated (BUTT, 2022).

According to the Landau-Levich equation, the thickness of the film formed is given by the Equation 4 below:

$$h = c \frac{(\eta U_0)^{\frac{2}{3}}}{\gamma^{\frac{1}{6}}(\rho g)^{\frac{1}{2}}} \text{ (Equation 4)}$$

where  $c$  is a constant,  $\eta$  is the solution's viscosity,  $U_0$  is the withdrawal speed,  $\gamma$  the surface tension of the liquid against air,  $\rho$  is the solution's density and  $g$  is the gravitational constant (AEGERTER and MENNIG, 2013).

By decreasing the withdrawal speed, the film thickness is decreased, as some of the solution flows back. However, one should not employ too low a withdrawal speed, because due to capillary forces more solution can be deposited in regions where the solvent has already evaporated. Consequently, the film may exhibit non-homogeneity (AEGERTER and MENNIG, 2013).

## 2.5 SPRAY DRYING

Spray drying is a process to produce solid particles by drying a fluid material. It is widely used since it is continuous, requires just a few preparation steps and also has a good control of the particles' crystallinity (or lack of it), morphology and size. Some other advantages are the possibility to synthesize a broad range of materials and production of very low waste (NANDIYANTO, et al., 2019).

Materials produced by spray drying are being applied in various areas. In the food industry, it is being used for the production of dried foods and in the pharmaceutical industry for the synthesis of drug active substances. In agriculture, it is being used in the manufacture of fertilizers, and in materials engineering it is being used to obtain ceramic particles (mainly because it can produce submicrometric or even nanometric particles), luminescent materials, and perovskites for energy

applications (NANDIYANTO, et al., 2019).

To understand the process, spray drying can be divided into three main stages: atomization, droplet-to-particle conversion and particle collection. The Figure 4 below illustrates the process.

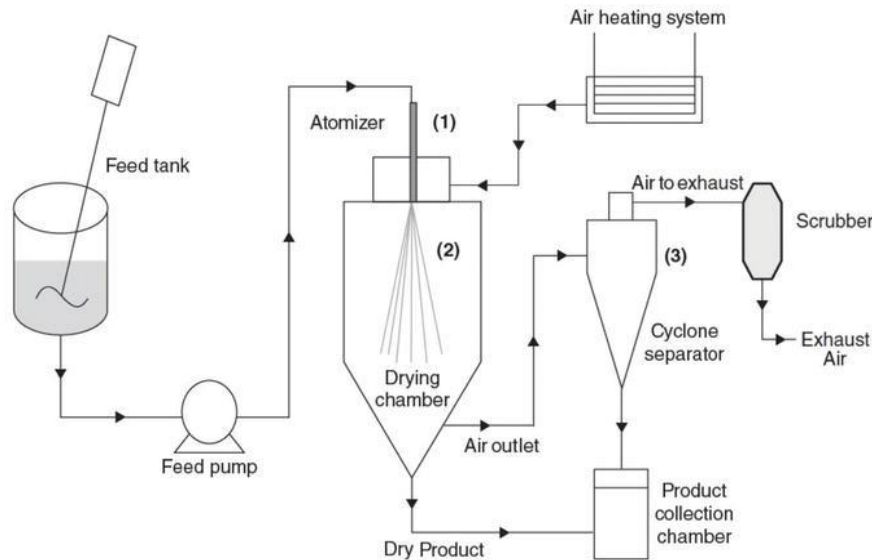


Figure 4: Scheme of the spray drying process steps (SANTOS, 2018).

The first and more important step is the atomization. It starts with breaking up the feed solution into smaller droplets, in order to enhance the next step, which is the drying chamber exposition. Due to the increase of surface area, the heat and mass transfer to dry the droplets is performed more efficiently and faster (SANTOS, 2018).

To obtain small droplets, the feed solution should have a lower surface tension or lower viscosity. It is also important to mention that the droplets are not all the same size, instead there is a distribution of sizes, which influences the drying of the particles and consequently their final characteristics (BOEL, et al. 2020).

Three types of atomizers are used mostly: with pressure nozzles, two-fluid nozzles, and rotary atomizers. In this work, the first one was used. It is capable of producing droplet size ranges from 20 to 200  $\mu\text{m}$ , depending on the relation between the applied pressure and the solution feed rate. For higher pressures, the droplets become smaller (BOEL, et al. 2020).

The next step will be responsible for removing the solvent, therefore obtaining dried particles, and can be divided into two main events: spray-air contact and droplet

drying step (NANDIYANTO, et al., 2019). In the drying chamber, a rapid moisture evaporation occurs through use of hot gas. The gas used can be either filtered atmospheric air or inert gas, depending on the material being synthesized. The size of the drying chamber should be appropriated, so that the particles have enough time to dry before reaching the chamber's wall (SANTOS, 2018). During the evaporation of the solvent, immediately after the contact between the gas and the droplet, the temperature of the droplet is immediately raised to the equilibrium evaporation temperature. Since the droplet is full of moisture, there is enough liquid in the droplet to replace the evaporated liquid, and thus evaporation occurs roughly at a constant rate. Evaporation proceeds at this constant rate until the formation of a thin shell, called a crust, once the solute dissolved in the liquid has reached saturation. For the drying process to proceed, the solvent diffuses from the core to the surface of the droplet, which occurs at a slower rate and leads to thickening of the crust. (NANDIYANTO, et al., 2019; PATEL, PATEL and SUTHAR, 2009).

Finally, the particles formed must be separated from the gas used for drying. The denser particles settle at the conical bottom of the drying chamber and can be collected using a filter. The finer particles, on the other hand, have an additional process of separation from the humid air, by means of external devices such as cyclone separator, bag filter or electrostatic precipitator. It is also possible to keep the gas temperature heated to around 100°C, in order to prevent condensation of substances and enable separation.

## 2.6 QUARTZ STRUCTURE AND LITHIUM EXCESS

Quartz has a very compact crystal structure, which enables interstitial substitution only under certain conditions.  $\text{Li}^+$  can occupy tunnel sites because of its small size and a fraction of  $\text{Si}^{4+}$  cations are replaced by  $\text{Al}^{3+}$  and  $\text{B}^{3+}$  in order to maintain charge neutrality. In addition, lithium ions are able to successfully stabilize the local charge due to the ideal valence and coordination number (XU, HEANEY and NAVROTSKY, 2001). This substitution also decreases the excess void space and thus stabilizes the high-temperature structure (LI, 1973). The name "Stuffed derivatives of quartz" is given to this family of materials with this charge-coupled substitution mechanism (XU, HEANEY and NACTEVROTSKY, 2001).



The stabilized phase depends on the mole fraction of  $\text{Si}^{4+}$  replaced by  $\text{Li}^+$  and  $\text{Al}^{3+}$  in the LAS system. When it is higher than approximately 0,65, low quartz (or  $\alpha$ -quartz) structure is crystallized. In the other hand, molar fractions smaller than 0,65 stabilizes high quartz (or  $\beta$ -quartz), which is normally the phase of greatest interest, since structures derived from this phase have a CTE near zero.  $\beta$ -eucryptite ( $\text{LiAlSiO}_4$ ), derived from  $\beta$ -quartz, when heated, practically does not vary in volume since the expansion in volume yield by the expansion in the (0 0 1) plane is canceled out by the shrinkage of the volume along the c-axis. . This property is verified on heating up to about 1473 K (XU, HEANEY and NAVROTSKY, 2001).

Zandora et al. evaluated the influence of small stoichiometric variations on the crystallization of LAS powders. In LAS glasses, the Li/Al ratio determines the connectivity of the glass. When this ratio is equal to 1, a polymerized glass is formed, because every  $\text{Li}^+$  is able to balance the charge ( $\text{Al}^{3+} + \text{Na}^+ \Leftrightarrow \text{Si}^{4+}$ ), as shown below in Figure 5. The excess lithium leads to the formation of non-bridging oxygens. This structural difference directly affects the crystallization of the material, since highly polymerized melts show small homogeneous nucleation rates and also possess excellent glass-forming ability (which means that they are more likely to form a glassy material). In this work, it was observed that non-bridging oxygens were likely to catalyze the crystallization, which involved just small structural arrangements of the amorphous network. Since the structure of the compositions without excess lithium was fully interconnected (polymerized), these rearrangements were only made possible with the increased energy provided by the temperature increase. In the compositions containing excess lithium, the formation of cristobalite was also suppressed, which is advantageous since this phase has a high coefficient of thermal expansion (ZANDONA, et al., 2021).

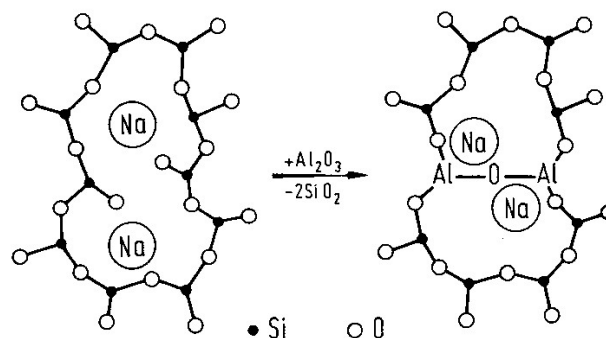


Figure 5: Network-forming character of  $\text{Al}_2\text{O}_3$  (SCHOLZE, 2013).

### 3 MATERIALS AND METHODS

#### 3.1 COMPOSITIONS

A sequence of solutions was analyzed in order to determine the composition with the highest potential to form Qss. Thus, a starting solution containing only SiO<sub>2</sub> precursors was used, and subsequently portions of a solution containing a mixture of Al<sub>2</sub>O<sub>3</sub> and CoO precursors were added step by step. Cobalt was chosen to replace lithium since this element showed promising results in a previous study (BAZZAOUI, et al, 2023). In this first step, the material was synthesized by dip coating due to the greater simplicity of the process.

To prepare the initial solution TEOS (99.9 %, Thermo Fisher) were added in a mix of ethanol (ROTIPURAN ≥ 99.8 %), distilled water and nitric acid (ORG Chemical, 1 mol/L), in stoichiometric proportions. The solution was homogenized for 5 minutes using a magnetic stirrer (IKA IKAMAG RCT). Lithium nitrate (LiNO<sub>3</sub> > 98 %, Merk), equivalent to 2.5 % mol SiO<sub>2</sub>, was added and the solution was homogenized once more. At the end, more ethanol was added to dilute the solution. For the Al<sub>2</sub>O<sub>3</sub> and CoO solution, aluminum nitrate nonahydrate (Al(NO<sub>3</sub>)<sub>3</sub>.9H<sub>2</sub>O ≥ 98 %, Thermo Fisher) and cobalt nitrate hexahydrate (Co(NO<sub>3</sub>)<sub>2</sub>.6H<sub>2</sub>O > 99 %, Thermo Fisher) were dissolved in ethanol. Ethanol was added so that the concentration of oxides in this solution and in the TEOS solution were equal. The nomenclature of the samples and the molar percentage of each oxide is shown in Table 1. In the nomenclature, the letter D indicates “dip coating” and the number indicates how many percent of SiO<sub>2</sub> was replaced by Al<sub>2</sub>O<sub>3</sub> and CoO.

Table 1: Composition of the solutions with different substitution percentages of SiO<sub>2</sub> by Al<sub>2</sub>O<sub>3</sub> and CoO.

Nomenclature	SiO <sub>2</sub> (mol%)	Al <sub>2</sub> O <sub>3</sub> (mol%)	CoO (mol%)
D0	100	0	0
D5	95.24	2.38	2.38
D9	90.90	4.55	4.55
D17	83.34	8.33	8.33
D20	80.00	10.00	10.00

D25	75.00	12.50	12.50
D33	66.66	16.67	16.67
D44	56.00	22.00	22.00
D50	50	25.00	25.00

Due to the results obtained in X-ray diffraction (XRD), the compositions with 20 % substitution (D20) and with 33 % substitution (D33) were evaluated. In these compositions, the effect of replacing lithium oxide by cobalt oxide in the formation of the quartz phase was evaluated.

For the D20 composition, the replacement of different percentages of lithium by cobalt was evaluated, which were 0 (corresponding to the composition  $\text{Li}_2\text{O}\cdot\text{Al}_2\text{O}_3\cdot 8\text{SiO}_2$  or LAS 8), 25, 50, 75 and 100 % (which corresponds to the composition D20 of Table 1 or  $\text{CoO}\cdot\text{Al}_2\text{O}_3\cdot 8\text{SiO}_2$ ). Therefore, a TEOS solution was prepared following the same steps mentioned before and aluminum nitrate nonahydrate was added in the end. This solution was divided into five solutions and, in which solution, a proper amount of lithium nitrate and cobalt nitrate hexahydrate, so that the molar percentage of oxides were according to Table 2. In the nomenclature, the number after the dot indicates how many percent of  $\text{Li}_2\text{O}$  was replaced by  $\text{CoO}$ . It's important to highlight that, due the valence of the ions, 1 mol of one mole of cobalt replaces 2 moles of lithium.

Table 2: Composition of the solutions D20 with different substitution percentages of  $\text{Li}_2\text{O}$  by  $\text{CoO}$ .

Nomenclature	$\text{SiO}_2$ (mol%)	$\text{Al}_2\text{O}_3$ (mol%)	$\text{Li}_2\text{O}$ (mol%)	$\text{CoO}$ (mol%)
D20.0	80.00	10.00	10.00	0
D20.25	80.00	10.00	7.50	2.50
D20.50	80.00	10.00	5.00	5.00
D20.75	80.00	10.00	2.50	7.50
D20.100	80.00	10.00	0	10.00

On the other hand, for the D33, the percentages of substitution of lithium by

cobalt investigated were 0 (which corresponds to the composition  $\text{Li}_2\text{O}\cdot\text{Al}_2\text{O}_3\cdot 4\text{SiO}_2$  or LAS4), 20, 33, 40, 45, 50, 67 and 100 % (which corresponds to the composition D33 of Table 1 or  $\text{CoO}\cdot\text{Al}_2\text{O}_3\cdot 4\text{SiO}_2$ ). The composition of the solutions, in molar percentage, is shown in Table 3. The procedure for preparing these solutions was the same as above, but instead of 5 solutions, 8 were prepared.

Table 3: Composition of the solutions D33 with different substitution percentages of  $\text{Li}_2\text{O}$  by  $\text{CoO}$ .

Nomenclature	$\text{SiO}_2$ (mol%)	$\text{Al}_2\text{O}_3$ (mol%)	$\text{Li}_2\text{O}$ (mol%)	$\text{CoO}$ (mol%)
D33.0	66.66	16.67	16.67	0
D33.20	66.66	16.67	13.33	3.34
D33.33	66.66	16.67	11.11	5.56
D33.40	66.66	16.67	10.00	6.67
D33.45	66.66	16.67	9.17	7.5
D20.50	66.66	16.67	8.34	8.33
D20.67	66.66	16.67	5.56	11.11
D20.100	66.66	16.67	0	16.67

To confirm the importance of adding excess lithium to the studied compositions, solutions of composition D33.100 with and without excess lithium were prepared and referred to as D33.100W and D33.100O, respectively.

For spray drying synthesis, the same D33 composition was also chosen to evaluate the formation of quartz with the progressive replacement of lithium by quartz. TEOS solution was prepared as mentioned before and aluminum nitrate nonahydrate was added to that solution. Lithium nitrate and cobalt nitrate nonahydrate were each separately dissolved in water. The solutions were then mixed to obtain the compositions with 0, 20, 33, 40, 50, 67, 80, and 100 % substitution of lithium for cobalt. The samples were respectively denominated S0, S20, S33, S40, S50, S67, S80 and S100 (the letter S refers to spray drying). Before the syntheses, the solution was dissolved in water, so that the solution would have a viscosity closer to that of water.

An additional solution was prepared and used both for spray drying and for dip

coating. In this case, instead of using ethanol, methanol (VWR Chemicals,  $\geq 99.9\%$ ) and nitric acid (Fluka,  $\geq 69,0\%$ ) were used. The molar percentages of the oxides were the same as for the samples D33.100 (Table 3). The sample synthesized by dip coating was denominated D100M and by spray drying, S100M. In this case, before the spray drying process, the solution was dissolved in methanol.

### 3.2 DIP COATING AND SPRAY DRYING

The dip coating process was performed using a controller Isel IMC1-10. The withdrawal speed chosen was 2.0 mm/s. The spray dryer was built up by combining an PALAS AGK 2000 atomizer (operated with 2.5 bar pressurized air), glass tubes, a filter holder and an oven, which was set at 400 °C.

### 3.3 HEAT TREATMENTS

The drying and heat treatment of the samples were carried out in a Vita Inceramat oven. Prior to the dip coating process, all glass substrates were annealed at 500 °C for 30 minutes in order to promote optimum adhesion of the deposited films (JONSSON and JONSON, 2010). All samples, whether produced by dip coating or spray drying, were after synthesis dried in the oven at 600 °C, and after that they were subjected to further heat treatments.

All the samples were heat treated from room temperature to 900 °C, with a heating rate of 10 K/min and a holding time of 30 minutes. The sample S0 were also heat treated at 800 °C, because at 900 °C a high amount of keatite solid solution (Kss) was formed, a phase that is not being studied and may cause shifting of the quartz phase peak. 5 samples of S100M were heat treated at 800, 850 °C, 900 °C, 950 °C and 1000 °C (one sample for each temperature) and the sample D100M was treated at 900 °C, but placed in the oven which was already at this temperature, where it was kept for only 10 minutes.

### 3.4 XRD AND HIGH TEMPERATURE XRD MEASUREMENTS

To determine the phases in the samples, XRD measurements were performed on a Malvern Panalytical Empyrean diffractometer, equipped with a Cu X-ray tube and a PIXcel 1D detector (255 channels, 14 mm active length). For the coatings, in order to avoid the intense signal from the substrate and obtain a more intense signal from

the coating itself, which is superficial, the equipment scan was performed with a fixed grazing incidence X-ray diffraction (GIXRD) angle equal to  $0.3^\circ$ . The incidence angle was varied from  $15^\circ$  to  $40^\circ$  and step size equal to  $0,03^\circ$ , a range that contains the main interference peak of Qss as well as that of the Spinel. The measurement range was reduced because for thin coatings, as in this case, the measurement is more challenging. The collected signal has a lower intensity, making the process time and cost demanding. For the powders, the measurement was carried out with an incidence angle ranging from  $10^\circ$  to  $90^\circ$  and a step size equal to  $0,03^\circ$ .

For the high temperature XRD (HT-XRD) measurements, Anton Paar's HTK 1200N heating chamber was used. The measurements were performed at temperatures of  $25^\circ\text{C}$ ,  $125^\circ\text{C}$ ,  $225^\circ\text{C}$ ,  $325^\circ\text{C}$ ,  $425^\circ\text{C}$ ,  $525^\circ\text{C}$ , and  $625^\circ\text{C}$ , with a heating rate of 10 K/min during heating between measurements.

### 3.5 SCANNING ELECTRON MICROSCOPY (SEM)

For the characterization of the material obtained by spray drying and after its thermal treatment, Zeiss EVO 50 scanning electron microscope equipment was used, operated at 10 kV.

### 3.6 TRANSMISSION ELECTRON MICROSCOPY (TEM)

The samples analyzed using the transmission electron microscope were dispersed in ethanol and deposited on carbon-coated copper grids. After this preparation, the measurements were conducted using a JEOL JEM2100 TEM, operated at 160 kV.

### 3.7 SAMPLE TRANSMISSION MEASUREMENTS

Regarding the optical characteristics of the samples, transmitted light measurements were conducted using the UV/Vis Spectrophotometer Analytik Jena SPECORD 200. The measuring range was from 100 to 1100 nm, with a step size of 5 nm.

### 3.8 THERMOGRAVIMETRIC ANALYSIS

Netzsch QMS 403C mass spectrometer and Netzsch STA 409 PC simultaneous thermal analyzer were used to determine how much weight is still lost

before crystallization and in the form of which gasses this mass is lost. The measurement was conducted at a heating rate of 10 K/min in an air atmosphere.

## 4 RESULTS

### 4.1 REPLACEMENT OF SiO<sub>2</sub> BY Al<sub>2</sub>O<sub>3</sub> AND CoO

To establish which compositions would be studied during this research, XRD measurements were carried out on samples with different percentages of SiO<sub>2</sub> replaced by Al<sub>2</sub>O<sub>3</sub> and CoO (Figure 6).

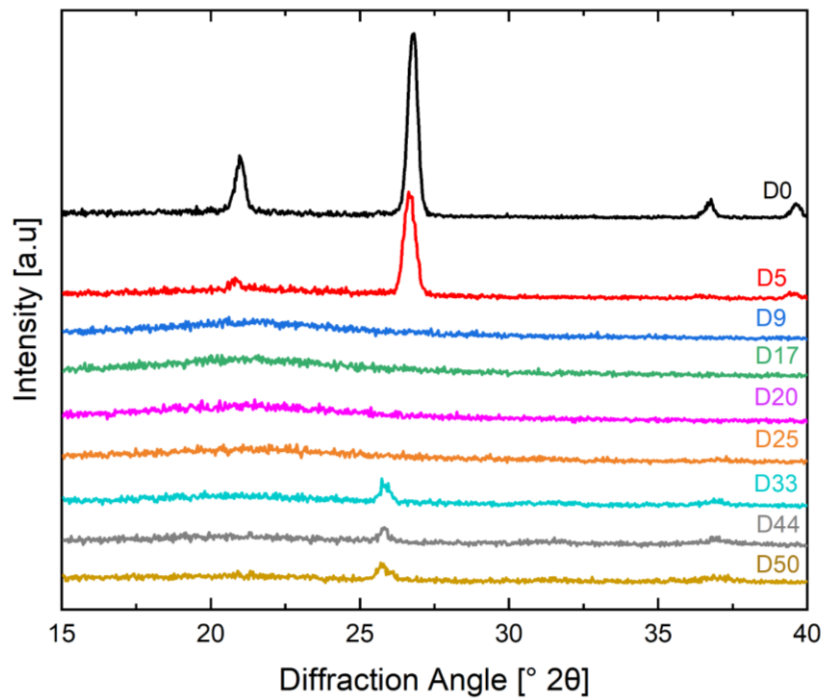


Figure 6: XRD patterns of the samples D0, D5, D9, D17, D20, D25, D33, D44 and D50.

From the interpretation of the interference patterns obtained by XRD measurement, the conclusion was drawn that quartz was formed for very small percentages of substitution (0 or 5 %) and for higher percentages of substitution (33, 44 and 50 %). For higher percentages, the peak has lower intensity, indicating that the percentage of quartz crystallized was low.

Compositions D20 and D33 were chosen for further investigation. Despite the fact that the first one did not form Qss, it was of great interest to understand the crystallization at intermediary substitution percentages. The second one was chosen since it displays a more intense peak, when compared to the samples with 44 and 50 % substitution.

Although the D20 composition did not show the formation of the Qss, previous



works (ZANDONA, et al., 2021) have shown that this phase can be obtained in glass-ceramics of the LAS 8 system, if the glass is appropriately heat treated.

#### 4.2 REPLACEMENT OF $\text{Li}_2\text{O}$ BY $\text{CoO}$ IN THE COMPOSITION D20

Therefore, starting from the  $\text{Li}_2\text{O}\cdot\text{Al}_2\text{O}_3\cdot 8\text{SiO}_2$  system, the substitution of lithium for cobalt was studied. The complete (100 %) substitution of lithium by cobalt corresponds to the D20 composition. In order to determine the effect of the substitution on the phases present in the samples after heat treatment, XRD measurements were performed (Figure 7).

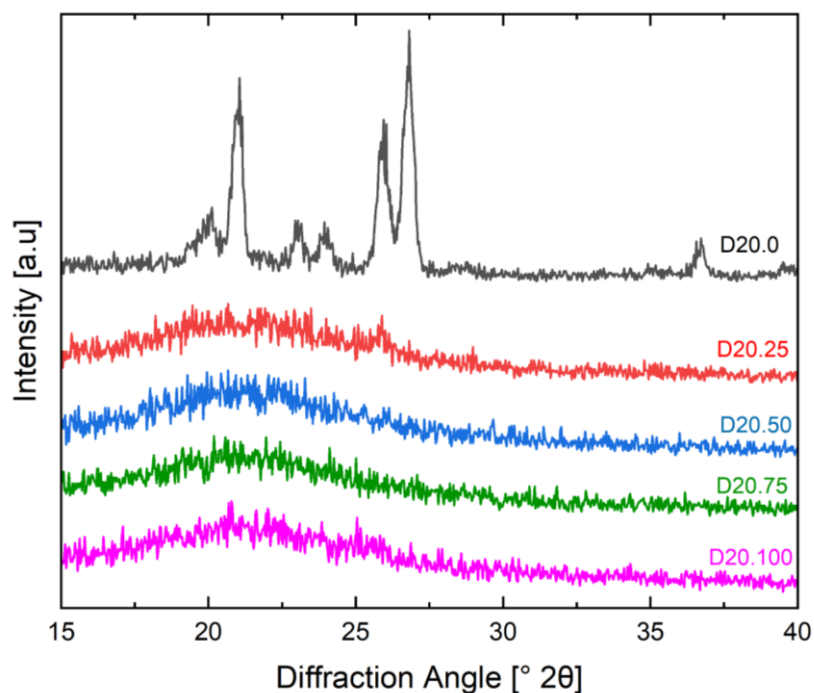


Figure 7: X-ray diffraction patterns of the samples D20.0, D20.25, D20.50, D20.75 and D20.100.

XRD measurements confirmed that it is possible to form the Qss phase in the LAS 8 system under the conditions of the heat treatment employed. However, a slightest substitution of lithium by cobalt (25 %) already inhibits the formation of this phase, since no crystalline peaks were observed. Further substitution had the same effect. The glass hump was observed for samples D20.25, D20.50, D20.75 and D20.100, even after heat treatment at 900 °C for 30 minutes. In face of these results, no further measurements were conducted with the D20 composition.

### 4.3 REPLACEMENT OF $\text{Li}_2\text{O}$ BY $\text{CoO}$ IN THE COMPOSITION D33

Starting from the  $\text{Li}_2\text{O}\cdot\text{Al}_2\text{O}_3\cdot 4\text{SiO}_2$  system, the effect of replacing cobalt by lithium in composition D33 was evaluated analogously to the one investigated for composition D20. Since it was shown previously that for composition D33 it is possible to crystallize Qss (Figure 6), a higher number of different substitution percentages were evaluated. Therefore, XRD measurements were performed (Figure 8).

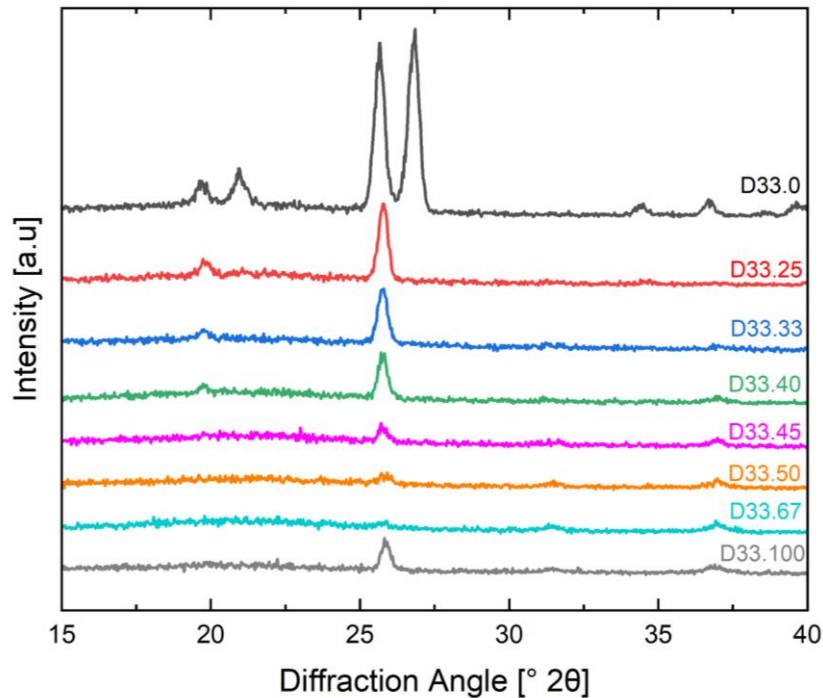


Figure 8: X-ray diffraction patterns of the samples D33.0, D33.25, D33.33, D33.40, D33.45, D33.50, D33.67 and D33.100.

As expected, due to previous studies (LÖSCHMANN, et al., 2022; ZANDONA, et al., 2020) for composition D33.0 ( $\text{LAS 4}$  or  $\text{Li}_2\text{O}\cdot\text{Al}_2\text{O}_3\cdot 4\text{SiO}_2$ ) high quartz was formed. With the increasing substitution of lithium for cobalt, a progressive decrease in the intensity of the peak relative to the quartz phase was observed, indicating that this phase is being formed in smaller quantities. For compositions D33.50 and D33.67 no quartz phase was formed. However, for the sample with complete replacement D33.100, Qss phase was formed, as previously verified (Figure 6).

### 4.4 LITHIUM EXCESS EFFECT

XRD measurements were also performed (Figure 9) to evaluate crystallized

phases of the samples D33.100W and D33.100O, in order to verify the need for the addition of excess lithium in the compositions under study.

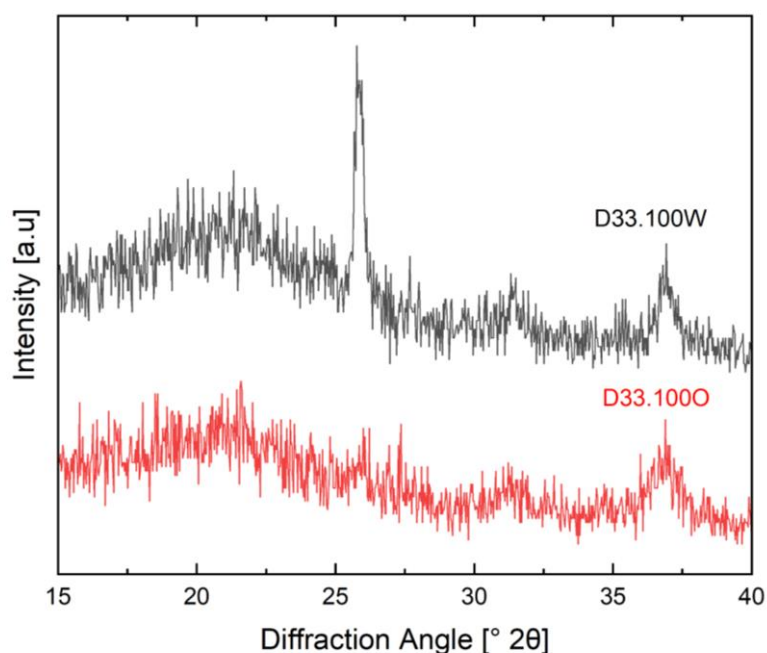


Figure 9: XRD results for the samples D33.100O and D33.100W.

For the D33.100O samples, no quartz peak was present, while for D33.100W, this phase was crystallized. In both patterns, it is possible to identify Spinel (peak at approximately 36.9 °). This result proves that a minimal addition (2.5 %mol) of lithium in excess (with respect to the stoichiometric composition) is necessary for the formation of Qss.

#### 4.5 REPLACEMENT OF $\text{Li}_2\text{O}$ BY $\text{CoO}$ IN SPRAY-DRIED POWDER

Since composition D33 was the composition with the best results for dip coating, it was also chosen for synthesis by spray drying. The effect of replacing Li by cobalt was similarly evaluated. The powders obtained by spray drying are shown in Figure 10.

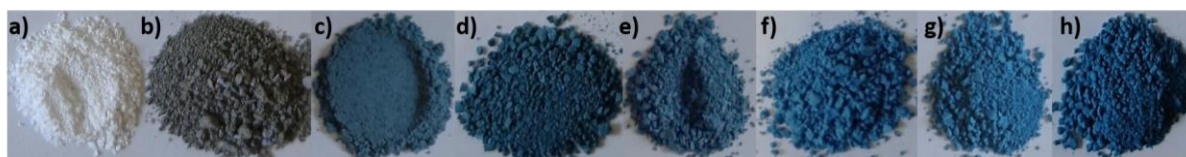


Figure 10: Powders obtained by spray drying of the solutions: a) S0, b) S20, c) S33, d) S40, e) S50, f) S67, g) S80 and h) S100.

In Figure 10 it is possible to visualize the powders obtained for the different compositions. The powder with no cobalt in its composition (which is the LAS 4 composition) is white, while, with just a small replacement of Li by cobalt (sample S20), the color of the powder becomes grayish. With further substitution, the powder's color changes to blueish.

XRD analyses were conducted (Figure 11) to determine the phases crystallized in the samples.

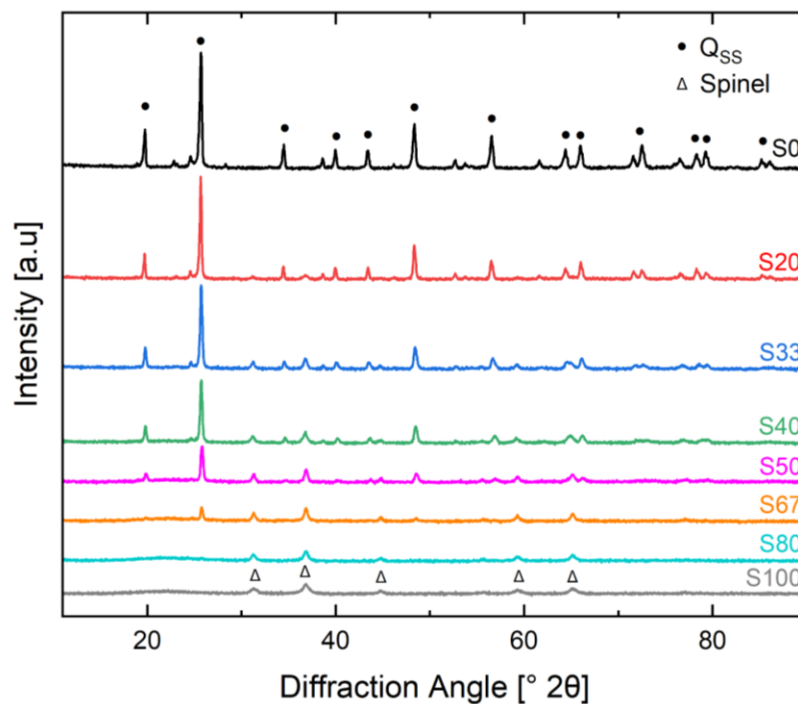


Figure 11: XRD patterns of the samples S0, S20, S33, S40, S45, S50, S67, S80 and S100.

Analyzing the curves obtained in the XRD measurements, it is possible to visualize that Qss peaks become progressively smaller (less intense) with the increasing of lithium replacement, which means that less Qss is being crystallized. For substitutions greater than 67 %, no Qss is formed, the only phase formed is Spinel. The diffraction pattern indicates that no Qss was formed for 100 % substitution, as was verified for the sample with the same composition synthesized by dip coating. Spinel is already formed for small replacement percentages (20 %) and the peaks attributed to this phase become increasingly more intense as the percentage of substitution increases.

#### 4.6 INFLUENCE OF THE SOLVENT USED FOR SPRAY DRYING

In order to verify if the solvent has any effect on which phases crystallizes after heat treatment, the spray drying solution was prepared using methanol. The powder obtained, as well as the powders after heat treatment at different temperatures, are shown in Figure 12.



Figure 12: Powders produced by spray drying of the solution S100M a) as-sprayed, b) after drying at 600 °C and after heat treatment at c) 800 °C, d) 850 °C, e) 900 °C, f) 950 °C and g) 1000 °C.

From the images above, it is possible to visualize that the as-received powder is light pink. However, when it is dried, its color changes to gray. With the heat treatment at 800 °C, the color remains the same, but changes again to violet for heat treatments at temperatures higher than 800 °C. When the powder is heat-treated at 950 °C and 1000 °C, it becomes blueish, which can indicate the crystallization of Spinel. In order to determine the phases crystallized, XRD measurements were conducted (Figure 13 e 14).

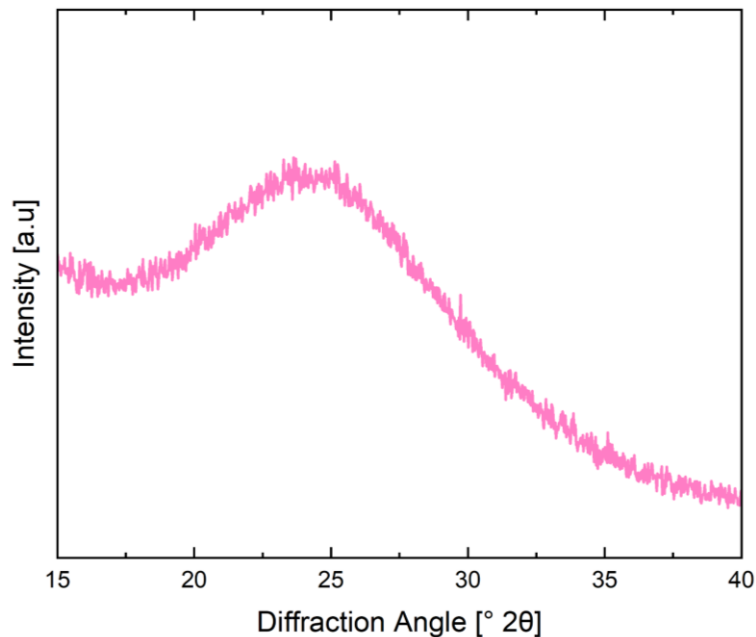


Figure 13: X-ray diffraction patterns of the as-sprayed S100M sample.

From the XRD pattern, it was possible to confirm that the material produced is a glassy powder, since a glass hump and no crystalline peaks were observed.

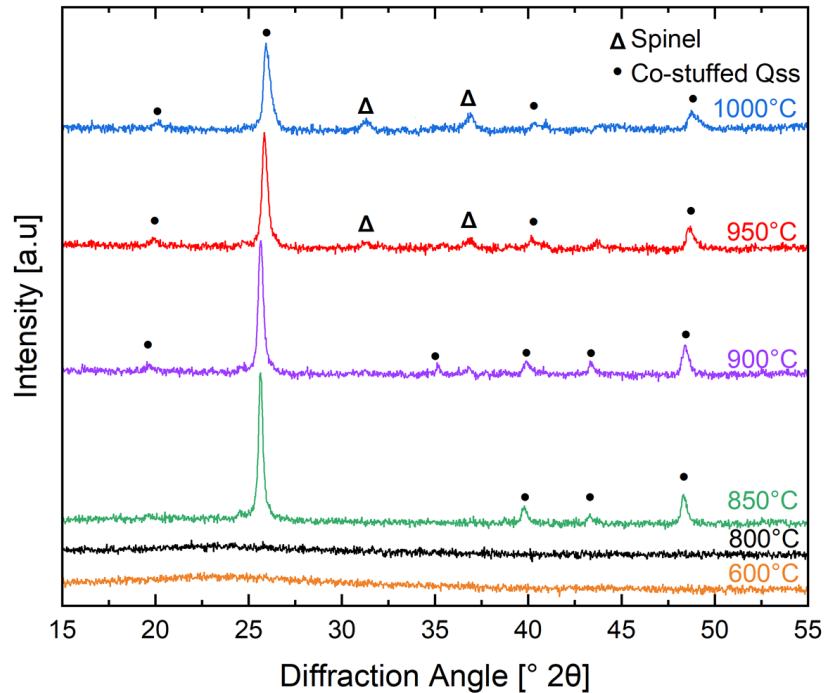


Figure 14: X-ray diffraction patterns of the sample S100M a) dried at 600 °C, and heat-treated at c) 800 °C, d) 850 °C, e) 900 °C, f) 950 °C and g) 1000 °C.

Based on the curves above, it can be stated that the material remains in the glassy state after drying and after heat treatment at 800 °C. It is possible to identify peaks which correspond to Qss, when the samples are heat-treated in temperatures above 800 °C. In the samples treated at 950 °C and 1000 °C, it was possible to verify the reduction of the peaks referring to the Qss phase, indicating that this phase was formed in smaller quantities. In the same temperatures that this decrease occurs, it is possible to observe the formation of the Spinel phase. These results are congruent with the assumptions made based on the color changes shown in Figure 12.

#### 4.7 XRD AND TRANSMISSION MEASUREMENTS OF D100M SAMPLES

The solution prepared for spray drying (sample S100M) was first used for synthesis by dip coating, so that the composition is not an influential variable in the comparison between the synthesis routes. In order to obtain a more intense signal for the measurements, i.e., a thicker coating, the glass substrate was coated 6 times. The sample, which was heat treated at 900 °C is shown in Figure 15 below.



Figure 15: Dip-coated samples produced with the same solution as sample S100M.

It is possible to notice that this sample has an intermediate color between blue and violet. To determine the phases in this sample, XRD measurements were performed (Figure 16).

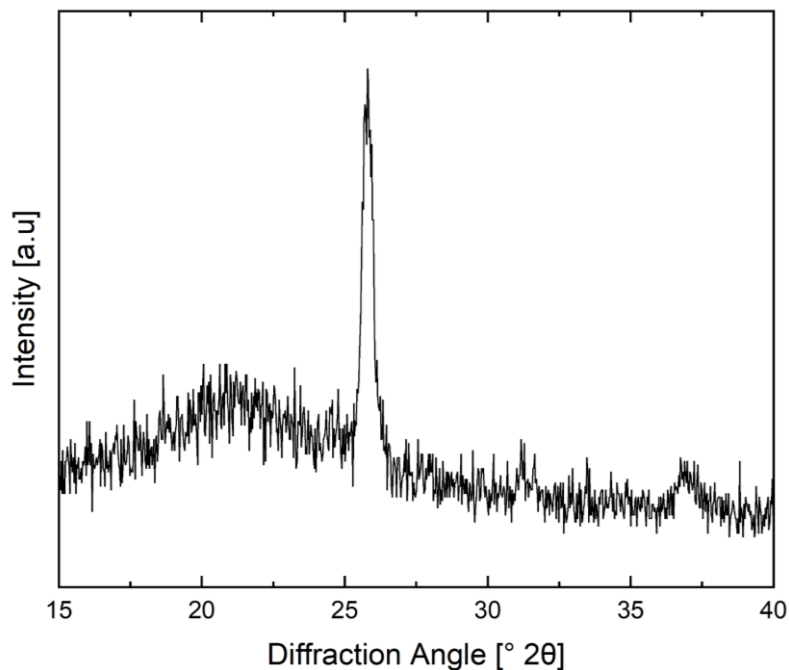


Figure 16: Dip-coated sample (D100M) produced with the same solution as the sample S100M.

As well as in the sample D100M, the diffraction pattern of the sample S100M showed that Qss was crystallized. In this sample, Spinel was also crystallized, in a minor quantity.

Transmission measurements were also conducted, as specified in section 3.6, and the results are shown in Figure 17.



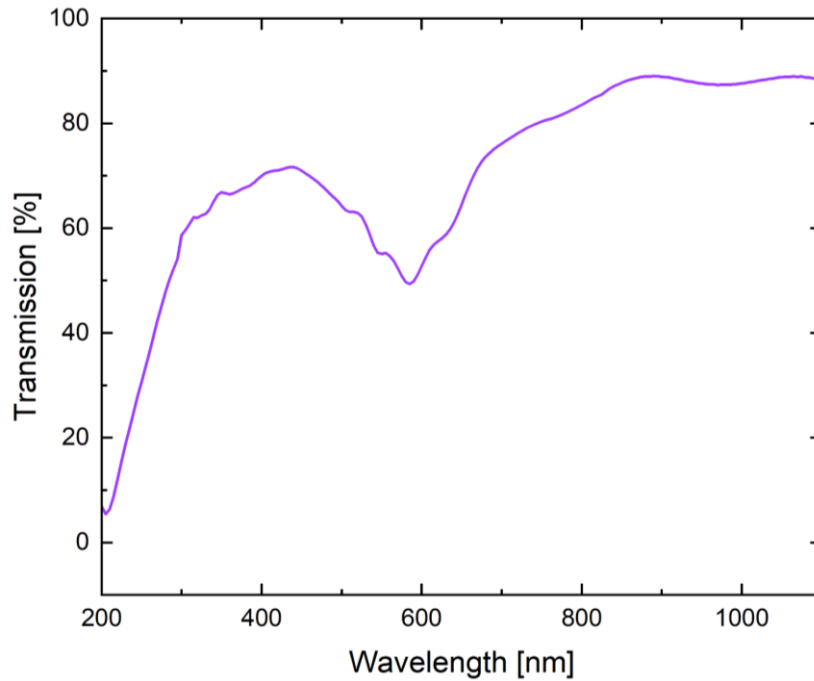


Figure 17: Transmittance of the sample D100M.

From the curve above, it is possible to conclude that more than 80 % of the radiation with a wavelength in the infrared range (between 700 and 1100 nm) is transmitted, which means that heat can be transmitted through this coated glass. In contrast, most of the UV radiation is not transmitted. In the visible range, there is a decay in the transmitted radiation around 600 nm. The absorption of these wavelengths, which corresponds to green, yellow and orange wavelengths, explains why the coating has a color between violet and blue.

#### 4.8 SCANNING ELECTRON MICROSCOPE (SEM) AND TRANSMISSION ELECTRON MICROSCOPE (TEM)

The size and the form of the powder prepared by spray drying and heat-treated at 800 °C, 900 °C and 1000 °C was investigated by SEM, as shown in Figure 18.



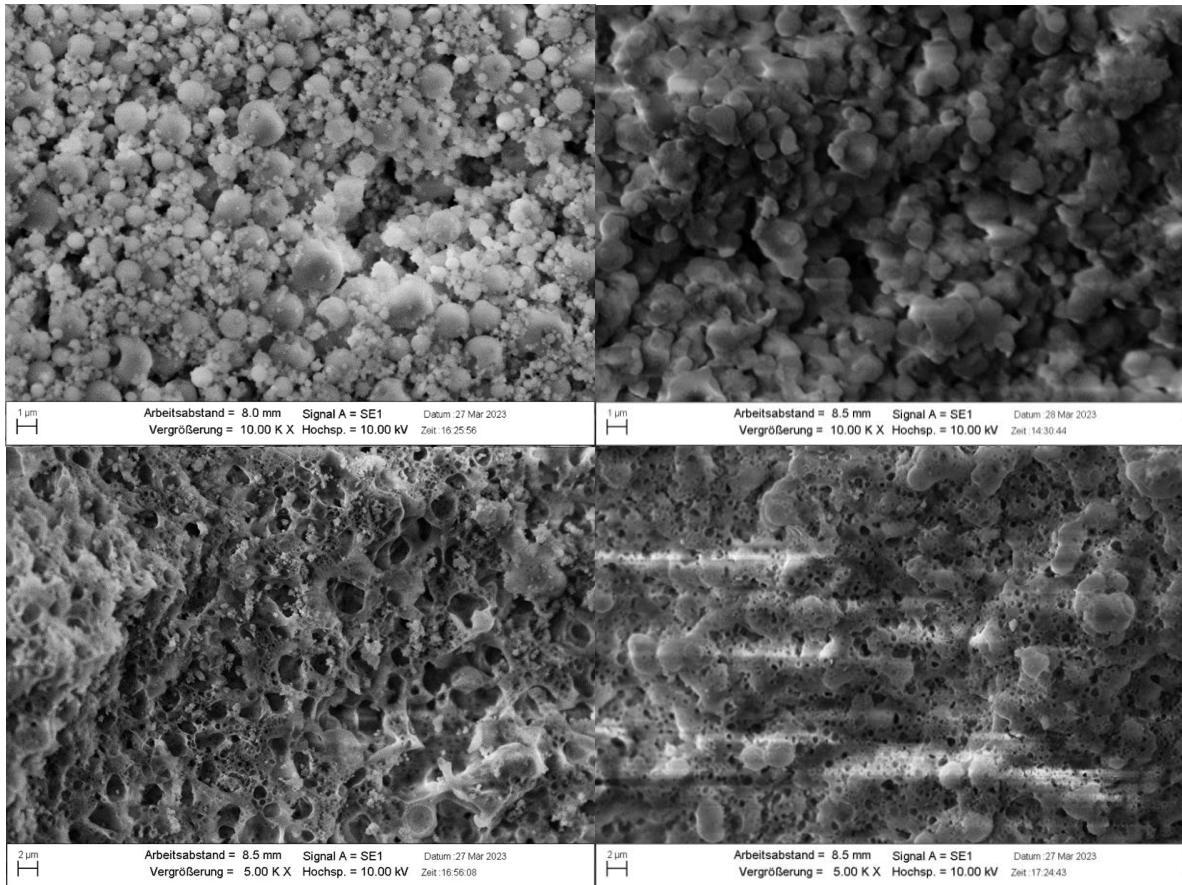


Figure 18: SEM images from the samples S100M a) as-sprayed and heat-treated at b) 800 °C, c) 900 °C and d) 1000 °C.

From Figure 18a, it is possible to conclude that nano-beads of various sizes were produced by spray drying. The nanobeads presented a wavy surface and there are signs of a collapse towards the interior in the surface of some of the bigger particles. For more insightful analysis of the powder prepared by spray drying, the as-sprayed powder was analyzed by TEM (Figure 19). Through TEM, it was possible to better visualize the powder single particles, which are spherical shaped. To measure the particle size of the powder prepared by spray drying, the software ImageJ was used (Figure 20). The S100M powder prepared by spray drying has a wide distribution, with the particle size varying between 20 to 3300 nm. 50 % of the particles are smaller than 320 nm and 50 % are bigger. With the heat treatment of the powder at 800 °C, the growth of the particles was verified and it has become difficult to identify unitary particles (Figure 18b). At this temperature, there was possibly a certain degree of sintering of the particles. The powder heat-treated at 900 °C presents a foam aspect (Figure 18c), which can be associated with the formation of bubbles. With the increase of temperature, the powder must have a greater degree of sintering and there was

crystallization of the Co-stuffed Qss phase, as identified by XRD (Figure 14). In Figure 18d, with sintering and crystallization of the Co-stuffed Qss and Spinel, the material has larger grains and smaller pores.

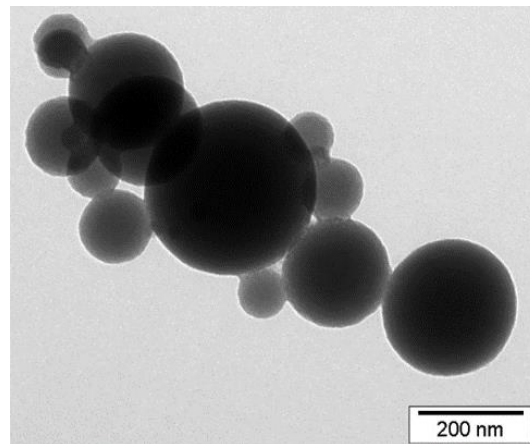


Figure 19: TEM image from as-sprayed S100M powder.

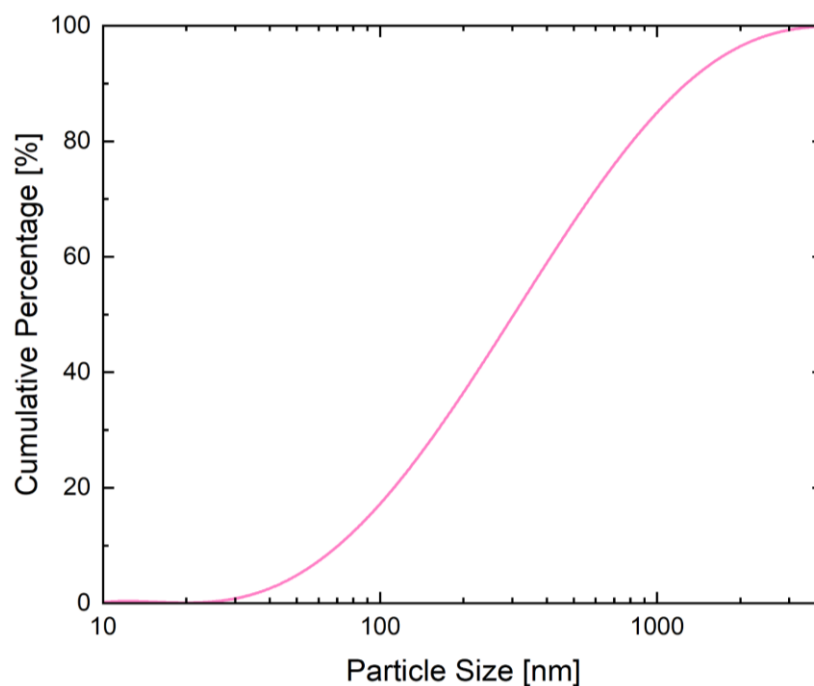


Figure 20: Particle size distribution of the as-sprayed S100M sample.

#### 4.9 THERMOGRAVIMETRIC ANALYSIS AND DIFFERENTIAL THERMAL ANALYSIS OF THE S100M POWDER

To better analyze the events that occur with the material during drying and heat treatments, a thermogravimetric analysis of the S100M sample prepared by spray drying was performed (Figure 21). Differential thermal analysis (DTA) was also used for the thermal characterization of the sample (Figure 22).

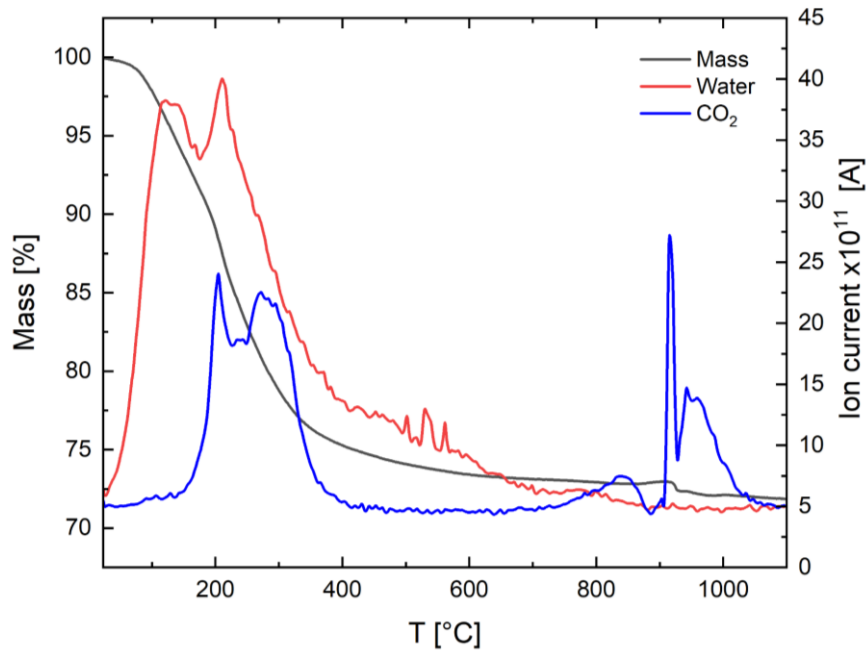


Figure 21: Thermogravimetric signal and mass spectrometry of the as-sprayed S100M sample.

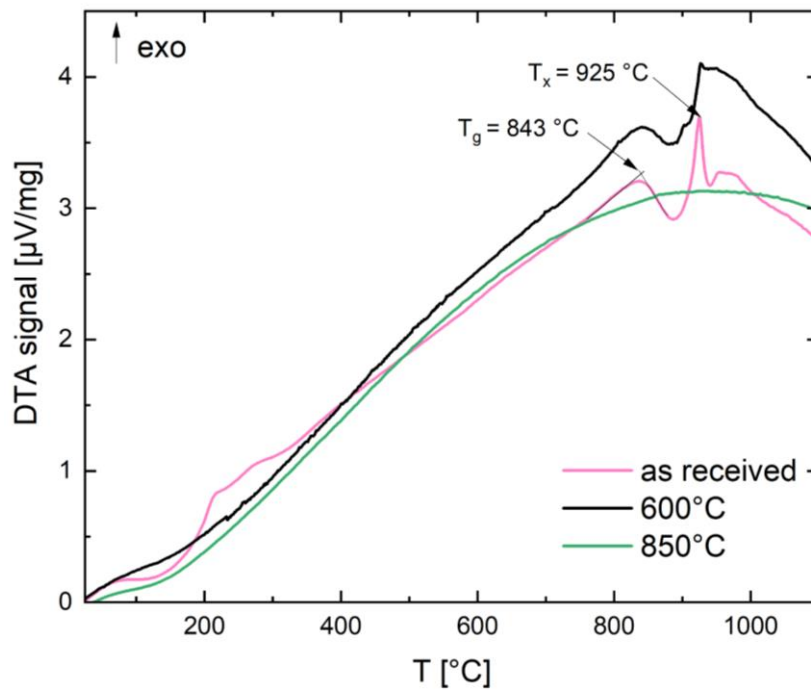


Figure 22: Differential thermal analysis (DTA) performed on samples S100M as-sprayed, dried at 600 °C and heat-treated at 850 °C.

The heat treatment of the material at 1100 °C results in approximately 27 % loss of mass, essentially in the form of H<sub>2</sub>O and CO<sub>2</sub>. The water is eliminated mostly between 150 °C and 250 °C, and at 600 °C, it has almost completely evaporated. CO<sub>2</sub>

is instead partially between 200 °C and 400 °C and also between 800 °C and 1050 °C.

An endothermic step in the DTA curve (Figure 22) is associated with the T<sub>g</sub> of this glass, which is 843 °C, and an exothermic peak (T<sub>x</sub> = 925 °C) is attributed to the crystallization of the powder. In the curve for the sample dried at 600 °C, T<sub>g</sub> and T<sub>x</sub> were still clearly visible. Meanwhile, it can be assumed that crystallization has already mostly occurred in the material annealed at 850 °C, since no thermal event was noticeable.

#### 4.10 THERMAL EXPANSION BY HIGH-TEMPERATURE X-RAY DIFFRACTION

The thermal expansion of Qss was analyzed in-situ by high-temperature XRD. These measurements were performed with automatic sample height correction. First, the behavior of the main Qss diffraction peak was studied for the sample S0 (which corresponds to the composition  $\text{Li}_2\text{O}\cdot\text{Al}_2\text{O}_3\cdot 4\text{SiO}_2$  or LAS 4). Before the measurements, the sample was heat-treated at 800 °C, a temperature at which less Keatite is formed. The measurements are shown in Figure 23.

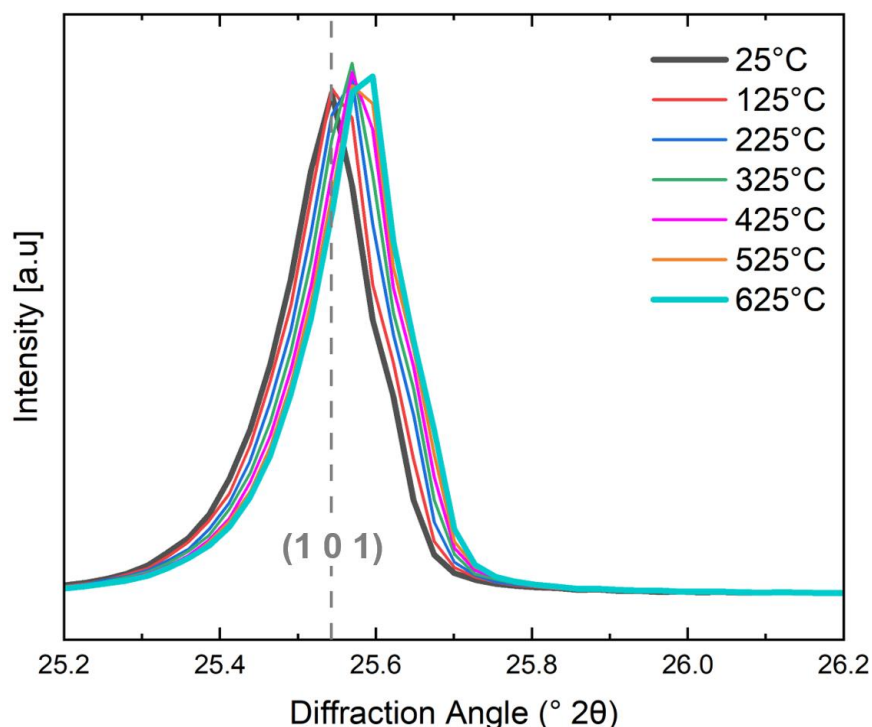


Figure 23: High-temperature X-ray diffraction measurements for samples S0.

The XRD measurements above revealed a shift in the peak position to higher

$2\theta$ , with the increase in temperature. Usually, with the increase in temperature, the displacement to smaller values of  $2\theta$  is observed, as a function of the expansion of cell volume. However, as mentioned in Theoretical Fundamentals, section 2.2, Li stuffed HQss crystallized in the LAS system displays a negative CTE, which explains why the peaks shifted to higher values.

Subsequently, thermal expansion of Qss was measured for the sample S100M (Figure 24).

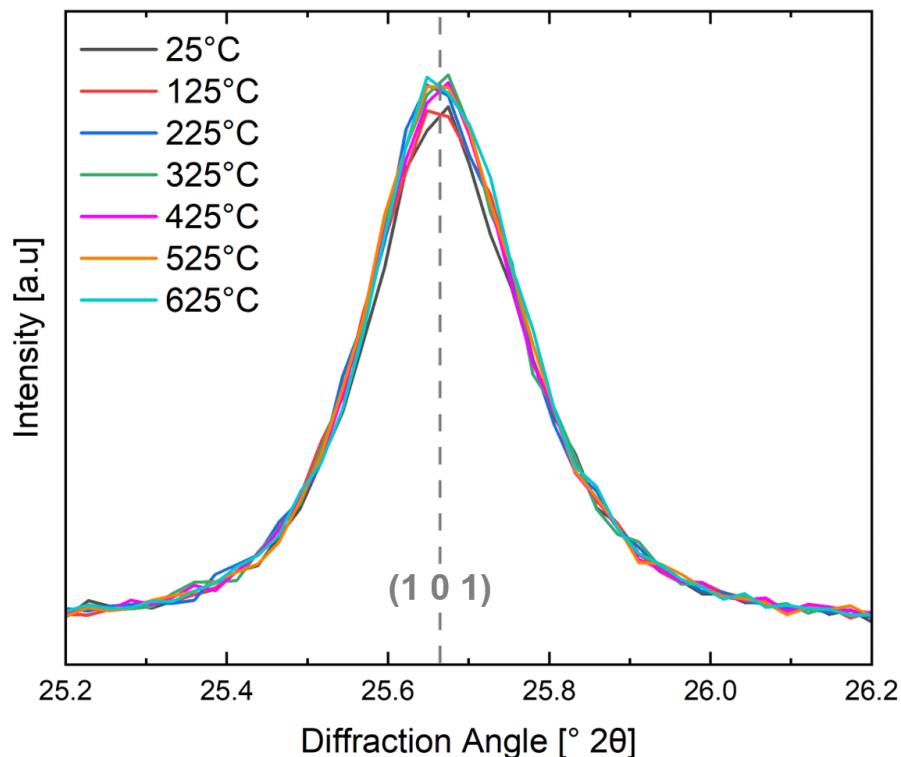


Figure 24: High-temperature X-ray diffraction measurements for samples S100M.

The diffraction patterns above show a different behavior of the Qss that was observed for the sample S0. From Figure 24, it is not possible to detect any shift in the peak position, which indicates that the cell volume of Qss does not expand during heating for the sample produced by spray drying.

Finally, the thermal expansion of Qss crystallized in the D100M sample heat treated at 900 °C was also measured (Figure 25).

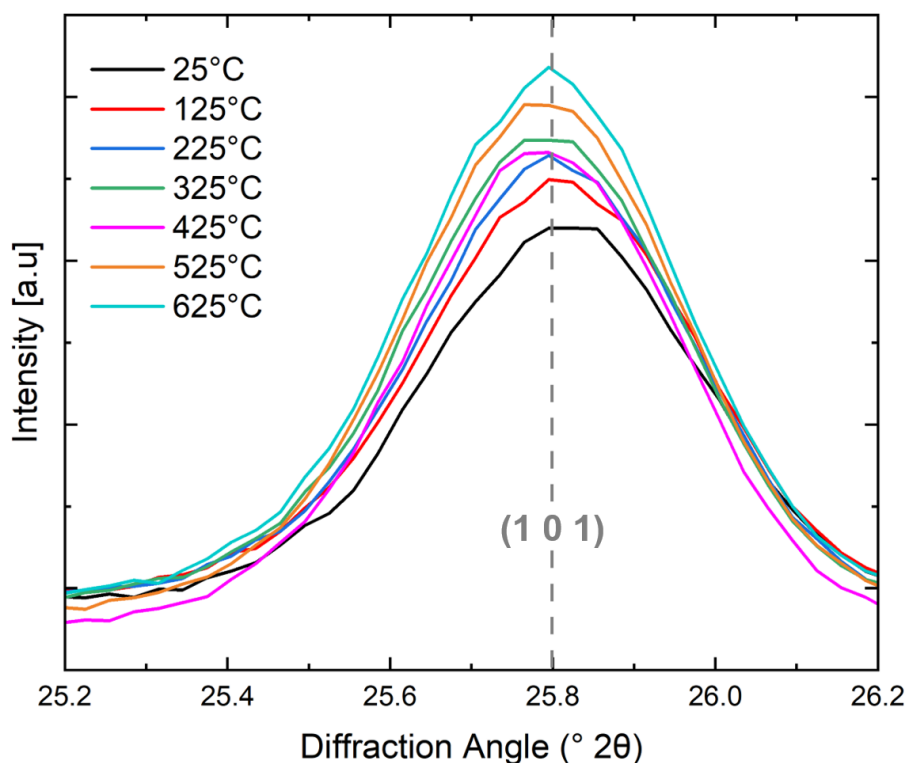


Figure 25: High-temperature X-ray diffraction measurements for samples D100M.

From the patterns above, it is possible to assume that there is a negligible shift in the peak position, which indicates a thermal expansion of the cell volume close to zero, in a similar way to what was observed for the spray-dried sample.

#### 4.11 COMPARISON OF Li- AND Co-STUFFED QSS BY XRD

To compare the Li-stuffed Qss, crystallized in the LAS4 sample treated at 800 °C, with the Co-stuffed Qss, crystallized in the S100M samples treated at 900 °C and 1000 °C, the powders were mixed with silicon standard powder. This material has a well-defined crystalline peak position (at 28.44 °), hence it was used to equalize the peak positions in all measurements performed with XRD, as shown in Figure 26. For greater accuracy of these results, the time per step was 2000 s.



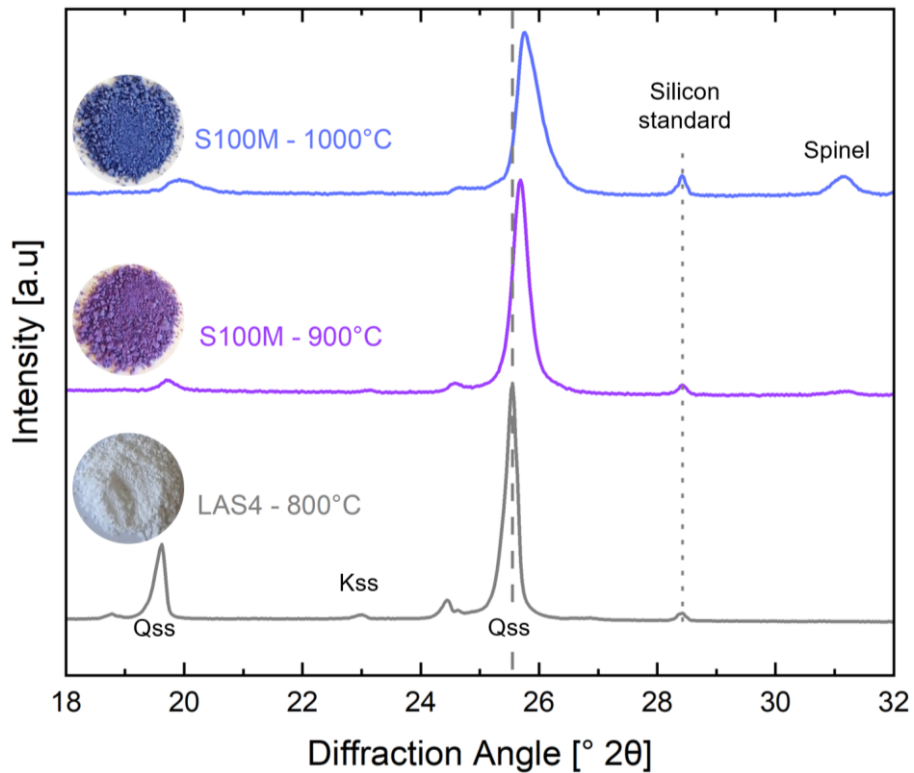


Figure 26: X-ray diffraction patterns from the samples LAS4 (heat-treated at 800 °C) and S100M (heat-treated at 900 °C and 1000 °C).

By comparing the curves of the samples LAS4 and S100M, heat-treated at 900 °C, it can be seen that the position of the peak referring to the Co-stuffed Qss phase shifts to higher  $2\theta$  values with respect to the position of the Li-stuffed Qss peak. With the increase of the heat treatment temperature of sample S100M to 1000 °C, the Co-stuffed Qss peak also shifts to higher  $2\theta$  values.

## 5 DISCUSSION

Co-stuffed quartz solid solution was successfully obtained, hence the synthesis methods used in this work were critical to the success of this work. Dip coating and spray drying produce sub-micron sized materials (layer and powder, respectively) with high area to volume ratios, which enables a high yield of surface crystallization and short annealing times. Therefore, the formation of a more stable phase, namely Spinel, is avoided (BAZZAOUI, et al., 2023). Regarding the compositional selection, it is noticeable a shift in the quartz peak position. For lower percentages of substitution, the peak position is around  $26.815^\circ$  and, for higher percentages, the peak position is at  $25.705^\circ$  (Figure 6). Considering that and the annealing conditions, the quartz crystallized in the first case was low quartz and in the second was Co-stuffed quartz. With 5 % substitution, Co probably segregated, but with the increase of this element in the glass, cobalt should have hampered the crystallization of quartz. With 33, 44 and 50 % substitution, the proportion between the elements of this glass enabled a network of interconnected tetrahedra created by  $\text{Si}^{4+}$  and  $\text{Al}^{3+}$  and stabilized by  $\text{Co}^{2+}$  (due to charge compensation).

For the D20.X compositions, even with a higher content of lithium, Co-stuffed quartz solid solution was not formed. Since the XRD patterns from the D20.25, D20.50, D20.75 and D20.100 showed a glass hump and no crystalline phases, the glass forming ability of these glasses is higher than that of D20.0. The samples were also heat-treated at higher temperatures (until  $1200^\circ\text{C}$ ) and for longer times (1 hour) and still no crystallization occurred.

The decrease of the peak intensity with the increasing replacement of  $\text{Li}_2\text{O}$  by  $\text{CoO}$  in the composition D33 indicates that the quartz crystallized does not bear cobalt. With 50 and 67 % substitution, the cobalt was within the Spinel structure and there was not enough lithium to stabilize the high quartz solution. For the D33.100, the peak corresponds to Co-stuffed quartz solid solution.

The solvent used has influenced not only the solution stability and homogeneity, but also the crystallization of the samples S100 and S100M (the first one did not crystallize Co-stuffed Qss) (Figures 11 and 14). It affects the viscosity of the solution, and thereby the particle formation (see Section 2.5). In aluminosilicates Qss structure



normally does not have great changes compared to the amorphous precursors and is formed as the first metastable devitrification phase (PETZOLDT, 1967). Hence, homogeneity and the structure formed during synthesis are crucial for the formation of quartz. Furthermore, the use of methanol might have been responsible for morphology of the particles (Figure 18a), which are wavy, not completely smooth and present cavities.

As related previously (BAZZAOUI, et al., 2023), with the substitution of Li by a heavier transition metal, the relative intensity of some diffraction peaks decreased significantly (Figure 14), specially at approximately  $19,5^\circ$  and  $34^\circ$   $2\theta$  ((010) and (110) reflections).

Thermogravimetric analysis (Figure 21) did not identify the loss of NO<sub>x</sub> gasses, proving that the spray drying conditions (400 °C and 2.5 bar) were able to fully decompose the nitrate salts used as precursors and synthesize a glass material. This result was confirmed by the absence of peaks in the XRD pattern of the as-sprayed S100M sample (Figure 13). Thermogravimetric analysis can also help understand the change of the color to black; it can be attributed to the graphitization of remaining organic precursors (TEOS, for example), since the release of CO<sub>2</sub> was detected even at high temperatures. The fact that T<sub>g</sub> and T<sub>x</sub> are in the temperature range in which the second CO<sub>2</sub> elimination event occurs corroborates with the assumption that this remaining gas is in the form of closed bubbles and/or dissolved in the glass structure. With the annealing of the samples at temperatures higher than 800 °C, the powder starts to crystallize, leading to the bubble collapse and CO<sub>2</sub> oversaturation in the residual glass and/or to bubble breakage.

Color in glass materials is a result of the selective absorption of light. In these materials, ions, atoms, or electrons present in the glass that can cause light absorption are called color centers. For light absorption to occur, there must be a transfer between the electronic levels of the color centers. Transition metals have incomplete 3d orbitals, making electronic transitions easier and absorbing light. Ions of different valence interact light differently, absorbing different wavelengths and therefore giving rise to different colors. In addition to valence, neighboring anions, molecules or neutral atoms (which are called ligands) near the cation also influence the wavelength of the absorbed light.

According to the ligand field theory, the d orbitals have 5 allowed orientations:  $d_{xy}$  (oriented between the x and y axes),  $d_{yz}$ ,  $d_{xz}$ ,  $d_{x^2-y^2}$  (oriented coincident with the x and y axes simultaneously),  $d_{z^2}$  (oriented coincident with the z axes). In octahedral coordination, the cation is surrounded by 6 anions, and in tetrahedral coordination, it is surrounded by 4 anions. Thus, the cation-anion distance is greater in tetrahedral than in octahedral coordination. Orbitals  $d_{x^2-y^2}$  and  $d_{z^2}$  are more influenced by the octahedral field and these orbitals will have their energies "raised". In the octahedral ligand field, the  $d_{xy}$ ,  $d_{yz}$  and  $d_{xz}$  orbitals have lower energy. The  $d_{x^2-y^2}$  and  $d_{z^2}$  orbitals are degenerate to each other, destabilized by the ligand field, and will have higher energy relative to the other orbitals (that is, the negative charge of the ligand will interact more with the positive charge). In the tetrahedral ligand field,  $d_{xy}$ ,  $d_{yz}$  and  $d_{xz}$  are closer to the ligands, and therefore will be destabilized (higher energy). The  $d_{x^2-y^2}$  and  $d_{z^2}$  orbitals are located between the ligands and are therefore more stabilized (lower energy). There is then an energy difference between the two different groups of d orbitals, which causes differences between the absorption spectra for different coordination around the cation (GRIFFITH and ORGEL, 1957).

Therefore, the color changes of the powder (excluding the black color due to graphitization) can be associated with the different structural configurations around cobalt (which has seven 3d electrons). In octahedral coordination, the  $\text{Co}^{2+}$  cation is surrounded by 6 anions and has three spin-allowed d-d transitions. The main absorption band occurs between 454 and 500 nm, yet has low intensity (DA SILVA, 1999). Thereby the pinkish hue of the as-sprayed powder can be attributed to  $\text{Co}^{2+}$  in octahedral coordination.

With the heat treatment of the sample at 850 °C, the change of the powder coloration to purple was observed and the crystallization of the Qss phase was verified by XRD. The purple color suggests an increasing contribution to the absorption due to the tetrahedrally coordinated  $\text{Co}^{2+}$ . In this configuration, there are two main absorption bands, with the band in the visible region between 500 and 625 nm. The absorption bands of Co in tetrahedral and octahedral coordination are close, with some overlap between them, and the first is about 100 times more intense than the second (DA SILVA, 1999). In agreement to that, BAZZAOUI et al. showed that  $\text{Co}^{2+}$  occupies both octahedral and tetrahedral sites in Qss. With the increase of the heat

treatment temperature (1000 °C), the powder turns blue, indicating the presence of  $\text{Co}^{2+}$  mainly in the tetrahedral coordination. As seen in the XRD pattern, Spinel is formed, in which tetrahedral coordination is largely preferred.

No secondary phases containing  $\text{Li}^+$  were identified in the samples in the XRD patterns in Figure 26, such as lithium disilicate or lithium metasilicate. By comparing the peak position of the Li-stuffed Qss with the peak position of the Co-stuffed, it is possible to conclude that the second one has a smaller cell volume than the first. Furthermore, the shift of the peak of the Co-stuffed Qss phase to higher  $2\theta$  was observed with the increase of the heat treatment temperature, which indicates the depletion of this phase in  $\text{Co}^{2+}$ . These observations indicate the preferential segregation of  $\text{Co}^{2+}$  in the  $\text{CoAl}_2\text{O}_4$  Spinel and the consequent enrichment of Qss in  $\text{SiO}_2$  and  $\text{Li}_2\text{O}$  (which was added to promote the crystallization of Qss).

To understand the thermal behavior of this crystal phase, it is essential to analyze its crystalline structure. Co-stuffed Qss crystals possess trigonal symmetry and cobalt ions occupy simultaneously tetrahedral and octahedral channel positions in it. The position of cobalt in the structure is uncertain due to inherent disorder of the channel sites, which also overlap (BEHRUZI and HAHN, 1977; BAZZAOU, et al., 2023).

The results of this study corroborate with the analyses by BAZZAOU, et al. Low or negative CTEs in Qss are mainly associated with the unit cell volume and not with the full hexagonal symmetry of aluminosilicates, referred to as HQss. According to the most recent conclusions in the literature, the thermal expansion of aluminosilicate glasses can be explained by the interaction of three structural mechanisms present in these glasses: (1) the slight deformation of Si or Al tetrahedra, (2) possible positional disordering of the cations in the channels with increasing temperature, which simultaneously stuffs tetrahedral and octahedral channels of the structure; and (iii) tetrahedral tilting, which is also the mechanism that enables low- to high-quartz transformation. It appears that the occupation of vacant channels sites, that may distort the trigonal framework, and greater available volume of framework sites in Al tetrahedra (compared to Si tetrahedra) enlarge the room-temperature quartz unit cell and reduce thermal expansion (XU et al., 2019; XU et al., 1999; BAZZAOU, et al.,

2023).

The combined channel disorder, crystalline site distortion and defective local charge balancing may partially account for the pronounced metastability of Qss, as previously speculated by other authors (XU et al., 2019; XU et al., 1999; BAZZAOUI, et al., 2023).

## 6 CONCLUSIONS/FINAL CONSIDERATIONS

In this work, we demonstrated that it is possible to obtain Co-stuffed Qss with near-zero thermal expansion between 25 °C and 625 °C. After dip coating different solutions with a wide range of compositions, the target one was determined to be  $\text{CoO}\cdot\text{Al}_2\text{O}_3\cdot 4\text{SiO}_2$ , since the XRD pattern of the sample D33 showed the more intense Qss peak. We also proved that it is necessary to add to that composition a small percentage of  $\text{Li}_2\text{O}$  (in this work, equivalent to the ratio  $\text{Li}/\text{Si} = 0,025$ ) to foster Qss crystallization.

An XRD study showed that the partial substitution of Li by Co in the LAS 4 (D33.0) system did not enable the crystallization of Co-stuffed (or Co- Li- stuffed) Qss, but induced the crystallization of Spinel. Co-stuffed Qss was only crystallized in D33.100, when all lithium was replaced by cobalt (neglecting Li excess).

With regard to spray drying, no Co-stuffed Qss was obtained in any sample when the solvent used was water. When the solvent used was methanol, a pinkish powder was obtained. With the heat treatment of the as-sprayed powder, the color changed to black, purple or blue, due to graphitization or to change of  $\text{Co}^{2+}$  coordination (octahedral to tetrahedral).

XRD patterns showed that  $\text{CoO}\cdot\text{Al}_2\text{O}_3\cdot 4\text{SiO}_2$  powder should be crystallized between entre 850 °C e 900 °C to prevent the segregation of Co to Spinel, maximizing the degree of filling of the target function Qss. Comparing spray dried and dip coating methods to obtain Co-stuffed Qss, the powder produced demonstrated greater relevance for material developers aiming to synthesize powders with zero thermal expansion.

As other authors already discussed, full hexagonal symmetry of Qss is not necessary to produce zero-thermal expansion materials. In Qss structure, cobalt occupies tetrahedral and octahedral channel positions and slightly deforms Si and Al tetrahedra.

Finally, this study demonstrated that sol-gel synthesis is a promising synthesis route to new zero-thermal expansion glass-ceramics powders and layers. Forthcoming works can make use of this route to assess the stuffing of Qss with other

ions. Additive manufacturing of glass-ceramic products using this material and sintering of this powder can also be an object of future researches.

## REFERENCES

AEGERTER, Michel Andre; MENNIG, Martin (Ed.). **Sol-gel technologies for glass producers and users**. Springer Science & Business Media, 2013.

AMSBECK, Lars; HELSCH, Gundula; RÖGER, Marc; UHLIG, Ralf; Development of a Broadband Antireflection Coated Transparent Silica Window for a Solar-Hybrid Microturbine System. In: SolarPACES. **SolarPACES 2009**, 15.-18. September 2009, Berlin, Germany. ISBN 978-3-00-028755-8.

BAZZAOUI, Haytem et al. Towards new zero-thermal-expansion materials: **Li-free quartz solid solutions stuffed with transition metal cations**. Journal of the European Ceramic Society, v. 43, n. 4, p. 1639-1648, 2023.

BOEL, Eline et al. Unraveling particle formation: From single droplet drying to spray drying and electrospraying. **Pharmaceutics**, v. 12, n. 7, p. 625, 2020.

BRINKER, C. Jeffrey et al. Sol—gel derived ceramic films—fundamentals and applications. **Metallurgical and ceramic protective coatings**, p. 112-151, 1996.

BUCHNER, Silvio et al. Comparison of the mechanical and tribological properties of a sintered low expansion Li<sub>2</sub>O–Al<sub>2</sub>O<sub>3</sub>–SiO<sub>2</sub> glass-ceramic and a commercial cooktop plate. **Glass Technology-European Journal of Glass Science and Technology Part A**, v. 54, n. 6, p. 211-217, 2013.

BUTT, Muhammad A. Thin-film coating methods: a successful marriage of high-quality and cost-effectiveness—a brief exploration. **Coatings**, v. 12, n. 8, p. 1115, 2022.

BEHRUZI, M; HAHN, T. Struktur und thermische Ausdehnung des ungeordneten β-Eukryptits, **Fortschr. Mineral**, v. 55, p. 12-13, 1977.

DAVIS, Mark J.; ZANOTTO, Edgar D. Glass-ceramics and realization of the unobtainable: Property combinations that push the envelope. **MRS Bulletin**, v. 42, n. 3, p. 195-199, 2017.

DA SILVA, MG Ferreira. The color change of aluminosilicate gel-derived glasses doped with CoO. **Materials research bulletin**, v. 34, n. 12-13, p. 2061-2068, 1999.

DEUBENER, J. et al. **Updated definition of glass-ceramics**. Journal of Non-Crystalline Solids, v. 501, p. 3-10, 2018.

DISLICH, Helmut; HUSSMANN, Eckart. Amorphous and crystalline dip coatings obtained from organometallic solutions: procedures, chemical processes and products. **Thin solid films**, v. 77, n. 1-3, p. 129-140, 1981.

DRESSLER, Martina; RÜDINGER, Bernd; DEUBENER, Joachim. An In Situ High-Temperature X-Ray Diffraction Study of Early-Stage Crystallization in Lithium Aluminosilicate Glass–Ceramics. **Journal of the American Ceramic Society**, v. 94,

n. 5, p. 1421-1426, 2011.

GRIFFITH, J. S.; ORGEL, L. E. Ligand-field theory. **Quarterly Reviews, Chemical Society**, v. 11, n. 4, p. 381-393, 1957.

HELSCHE, Gundula et al. Crystallization and quartz inversion temperature of sol-gel derived LAS solid solutions. **Journal of Non-Crystalline Solids**, v. 492, p. 130-139, 2018.

HOLLAND, Wolfram; BEALL, George H. **Glass-ceramic technology**. John Wiley & Sons, 2019.

KAJIHARA, Koichi. Recent advances in sol-gel synthesis of monolithic silica and silica-based glasses. **Journal of Asian Ceramic Societies**, v. 1, n. 2, p. 121-133, 2013.

KLEIN, L. C. Sol-gel processing of silicates. **Annual Review of Materials Science**, v. 15, n. 1, p. 227-248, 1985.

JONSSON, Andreas; ROOS, Arne; JONSSON, Emma K. The effect on transparency and light scattering of dip coated antireflection coatings on window glass and electrochromic foil. **Solar energy materials and solar cells**, v. 94, n. 6, p. 992-997, 2010.

LI, Chi-Tang. The role of lithium in stabilizing some high-temperature silica phases. **Zeitschrift für Kristallographie-Crystalline Materials**, v. 138, n. 1-6, p. 216-236, 1973.

LÖSCHMANN, Jessica et al. Accelerated crystal growth in a lithia aluminosilicate glass. **Acta Materialia**, v. 230, p. 117837, 2022.

MONTAZERIAN, Maziar; SINGH, Shiv Prakash; ZANOTTO, Edgar Dutra. An analysis of glass-ceramic research and commercialization. **Am Ceram Soc Bull**, v. 94, n. 4, p. 30-5, 2015.

NAKATSUKA, Akihiko et al. Cation distribution and bond lengths in CoAl<sub>2</sub>O<sub>4</sub> spinel. **Solid State Communications**, v. 128, n. 2-3, p. 85-90, 2003.

NANDIYANTO, Asep Bayu Dani et al. Template-assisted spray-drying method for the fabrication of porous particles with tunable structures. **Advanced Powder Technology**, v. 30, n. 12, p. 2908-2924, 2019.

PATEL, R. P.; PATEL, M. P.; SUTHAR, A. M. Spray drying technology: an overview. **Indian Journal of Science and Technology**, v. 2, n. 10, p. 44-47, 2009.

PETZOLDT, J. Metastabile Mischkristalle mit Quarzstruktur mit Oxidsystem Li<sub>2</sub>O-MgO-ZnO-Al<sub>2</sub>O<sub>3</sub>-SiO<sub>2</sub>, **Glastechnische Berichte** n. 40, p. 385-395, 1967.

REBOUÇAS, L. B. et al. Characterization of Li<sub>2</sub>O-Al<sub>2</sub>O<sub>3</sub>-SiO<sub>2</sub> glass-ceramics produced from a Brazilian spodumene concentrate. **Cerâmica**, v. 65, p. 366-377,



2019.

SciGlass: Glass Property Inform. Version 7.7. [S.I.]: AKos GmbH. Available at: <<http://www.akosgmbh.de/sciglass/sciglass.htm>>. Accessed: March, 30th 2023. SANTOS, Daniel et al. Spray drying: an overview. **Biomaterials-physics and chemistry-new edition**, p. 9-35, 2018.

SCHOLZE, Horst. **Glas: Natur, Struktur und Eigenschaften**. Springer-Verlag, 2013.

VARSHNEYA, Arun K. **Fundamentals of inorganic glasses**. Elsevier, 2013.

VOGEL, Werner. **Glasfehler**. Springer-Verlag, 2013.

XU, Chengjian et al. Future material demand for automotive lithium-based batteries. **Communications Materials**, v. 1, n. 1, p. 99, 2020.

XU, Hongwu et al. Structural behavior of a stuffed derivative of  $\alpha$ -quartz, Mg 0.5 AlSiO<sub>4</sub>, at high temperature: an in-situ synchrotron XRD study. **Physics and Chemistry of Minerals**, v. 46, p. 717-725, 2019.

XU, Hongwu et al. Structural mechanisms underlying near-zero thermal expansion in  $\beta$ -eucryptite: A combined synchrotron x-ray and neutron Rietveld analysis. **Journal of Materials Research**, v. 14, n. 7, p. 3138-3151, 1999.

XU, H.; HEANEY, Peter J.; NAVROTSKY, A. Thermal expansion and structural transformations of stuffed derivatives of quartz along the LiAlSiO<sub>4</sub>-SiO<sub>2</sub> join: a variable-temperature powder synchrotron XRD study. **Physics and Chemistry of Minerals**, v. 28, p. 302-312, 2001.

ZANDONA, Alessio; HELSCH, Gundula; DEUBENER, Joachim. Inversion of quartz solid solutions at cryogenic temperatures. **Journal of the American Ceramic Society**, v. 103, n. 11, p. 6630-6638, 2020.

ZANDONA, Alessio et al. Spray-dried TiO<sub>2</sub> (B)-containing photocatalytic glass-ceramic nanobeads. **Advanced Functional Materials**, v. 31, n. 8, p. 2007760, 2021.

ZANDONA, A. et al. The effects of a Li<sub>2</sub>O excess on the crystallization sequence of lithium aluminosilicate glass powders. **Journal of Non-Crystalline Solids**, v. 561, p. 120748, 2021.

ZANOTTO, Edgar D.; MAURO, John C. The glassy state of matter: Its definition and ultimate fate. **Journal of Non-Crystalline Solids**, v. 471, p. 490-495, 2017.

ZANOTTO, Edgar Dutra. Bright future for glass-ceramics. **American Ceramic Society Bulletin**, v. 89, n. 8, p. 19-27, 2010.